UC Santa Barbara

UC Santa Barbara Electronic Theses and Dissertations

Title

Silicon Photonics for Harsh Environments

Permalink

https://escholarship.org/uc/item/3f05g3cf

Author

Estrella, Steven Brian

Publication Date

2022

Peer reviewed|Thesis/dissertation

eScholarship.org Powered by the California Digital Library
University of California

UNIVERSITY OF CALIFORNIA

Santa Barbara

Silicon Photonics for Harsh Environments

A dissertation submitted in partial satisfaction of the

requirements for the degree Doctor of Philosophy

in Electrical and Computer Engineering

by

Steven Brian Estrella

Committee in charge:

Professor Clint L. Schow, Chair

Professor Larry A. Coldren

Professor Galan Moody

Dr. Daniel S. Renner

June 2022

The Dissertation of Steven Brian Estrella is approved.

_____
Daniel S. Renner

_____
Galan Moody

_____
Larry A. Coldren

_____
Clint L. Schow, Committee Chair

June 2022

Silicon Photonics for Harsh Environments

Copyright © 2022

by

Steven Brian Estrella

ACKNOWLEDGEMENTS

I've been looking forward to writing this section of my thesis for so many years now, as I have received so much help, encouragement, love, and support from so many people to make this possible. First, I would like to thank my advisor Professor Clint Schow, who gave me an opportunity to pursue my lifelong dream of obtaining an Ph.D. I have received much support, encouragement, and advice from Clint as I navigated graduate school, work, and life in general. I would also like to thank my committee members: Professor Larry Coldren, Professor Galan Moody, and Dr. Daniel Renner, for agreeing to be a part of this journey. A special thanks goes to Daniel, who has been my manager and mentor for the last several years, and has allowed me many opportunities for growth in management, leadership, and business, in addition to appreciating fine cuisine on our business trips across the U.S. To my past and present research groupmates: Dr. Takako Hirokawa, Dr. Hector Andrade, Aaron Maharry, Stephen Misak, Yujie Xia, and Evan Chansky, thank you for making my graduate school experience so rich and enjoyable, and for working with me on many of my projects.

Special acknowledgement is needed for the founders of Freedom Photonics: Dr. Milan Mashanovitch and Dr. Leif Johansson. You both gave me the opportunity to dive into the wonderous field of photonics at a young age, trained me in nearly all aspects, and supported my goal of one day getting a Ph.D. After 13 years, this moment has finally arrived, and I am truly thankful for all the support and accommodations made for me over the past 6 years in graduate school. A special thanks goes to my team members Trevor Cooper and Thomas Dorch, who made very large contributions to this work. I am especially thankful to Thomas for agreeing to come work with me and be a part of this journey: I look forward to watching

your growth and know you will accomplish great things. To Don Kebort and Dr. Maddy Woodson, you both have been some of my closest colleagues and friends, and I appreciate all the time spent discussing life and working side-by-side with you over the years. You both have lent an open ear countless times of the years – thanks for the sage advice. To my current and former officemates, Devon Gavigan, Dr. Stewart "Tom" Fryslie, Tim Hambley, and Ryan Meschewski, thank you for listening to my wild ideas and life's problems, being a great audience for my various whiteboard "mini lectures", and also supporting my dream of getting a Ph.D. Thank you to Henry Garett and Juan Campero, for helping to assemble so many prototypes over the years. You are both truly unsung heroes in the packaging world. Also, thank you Dr. Gordon Morrison and Ken Hay, who have also helped me throughout my career, both on a technical and personal level. So many other colleagues from Freedom Photonics, both past and present, have been involved in this journey, and to you all I say thank you.

Thank you to my sponsors at the U.S. Army: Dr. Michael Gerhold, Dr. Jason Zeibel, Dr. Peter Smith, and Dr. Alex Brown, who have enabled much of this research. In addition, thank you to the U.S. Department of Energy, Office of Science: Dr. Helmut Marsiske, Dr. Maurice Garcia-Sciveres, and Alan Prosser, who have been very supportive and encouraging of this work. I have enjoyed working with you all over the past 6 years or so and will continue to work on maturing this technology.

A special thank you to my parents, George, and Celia Estrella. Both of my parents have worked so hard to ensure that I get access to nearly every opportunity possible to satiate my thirst for science. My father George gave me one of my first pieces of electronics to play with: a simple mercury switch from an old bi-metallic thermostat. You also taught me Ohms Law, at an age before I even learned multiplication and division. My mother Celia developed my

love for reading all things science, taking my youngest sister and I to the public library on a nearly weekly basis. After consuming all the “children’s science books”, you let my check out my first college electronics textbook around age 6: I had no idea what the book was saying, but I loved all the pictures / schematics of the circuits. Who would have known that a few decades later that it would become an essential part of my life? Thank you both, and I truly love you. To my three older siblings: Danette, Anthony, and Lisette, thank you for always being there for me throughout my life. I can honestly say that you all are my best friends, and each of you have had a unique impact on me growing up. I love you all.

Finally, a truly special thank you goes to my wife Viviana “Ingrid” Estrella. Before I even started the graduate school journey, you were such a big part of my life. We’ve experienced so much together during my graduate school time at UCSB: starting a business together, adopting two dogs, getting engaged, getting married during the COVID-19 pandemic, traveling the world together. You have been and remain such an important part of my life. Your love, support, and encouragement to pursue this degree has largely gone unseen to most; without it I would not be who I am today. Thank you for always being there for me, for picking me up when I was down, and just being the wonderful person that you are, day in and day out. I look forward to spending my life with you and writing the next chapters of our lives.

This material is based upon work supported in part by the U.S. Army, Army Research Office, under Contract Number W911NF18C0096, and in part by the U.S. Department of Energy, Office of Science, Office of High Energy Physics under Award Number DE-SC0020691.

VITA OF STEVEN BRIAN ESTRELLA
June 2022

EDUCATION

2022 (expected)	Ph.D. in Electrical Engineering, University of California, Santa Barbara
2018	M.S. in Electrical Engineering, University of California, Santa Barbara
2010	B.S. in Electrical Engineering, University of California, Santa Barbara

PROFESSIONAL EMPLOYMENT

2021-2022	Director of Business Development, Freedom Photonics
2019-2021	Quantum Technology & Applications Technical Leader, Freedom Photonics
2016-2019	Senior Photonics Design Engineer, Freedom Photonics
2010-2016	Design Engineer, Freedom Photonics
2009-2010	Intern R&D Engineer, Freedom Photonics
2007-2009	Intern Electrical Engineer, InTouch Health (now Teledoc Health)

SELECTED PUBLICATIONS

Estrella, Steven B., Thomas P. Dorch, and Daniel S. Renner. "Progress in Optical Interconnects for Harsh Environments." *Physics and Simulation of Optoelectronic Devices XXX*. Vol. 11995. SPIE, 2022.

Estrella, Steven B., Thomas P. Dorch, Trevor M. Cooper, Aaron Maharry, Takako Hirokawa, Daniel S. Renner, and Clint L. Schow. "Novel Link Architecture Minimizing Thermal Energy Dissipation for Cryogenic Optical Interconnects," in *Optical Fiber Communication Conference (OFC) 2021*, OSA Technical Digest (Optical Society of America, 2021), paper F2E.3. [Top-Scored]

Estrella, Steven B., Takako Hirokawa, Aaron Maharry, Daniel S. Renner, and Clint L. Schow. "High-speed silicon photonic optical interconnects for cryogenic readout (Conference Presentation)." *Optical Interconnects XX*. Vol. 11286. International Society for Optics and Photonics, 2020.

Estrella, Steven B., Daniel Renner, Takako Hirokawa, Aaron Maharry, Mario Dumont, and Clint Schow. “High-Speed Optical Interconnect for Cryogenically Cooled Focal Plane Arrays.” 18.1, *GOMACTech*, 2019.

AWARDS

Top-Scored Paper, Optical Fiber Communications (OFC) Conference, 2019

ECE Dissertation Fellowship, University of California, Santa Barbara, Spring 2022

ABSTRACT

Silicon Photonics for Harsh Environments

by

Steven Brian Estrella

Growing demands in high data capacity and low energy consumption have driven the development of high-performance optical interconnects for many commercial applications, such as links for long-haul, intra-/inter-datacenter, and 5G communication. Typically, the photonic devices used in these environments are optimized for operation at or above room temperature, however there is an existing and growing need for optimized photonic devices to operate in cryogenic and/or high-radiation environments. Applications of these optical interconnects range from control and readout from superconducting integrated circuits for quantum computing, to readout of tracking detectors in high-energy physics (HEP) particle accelerators, to readout of next-generation infrared (IR) focal plane array (FPA) detectors.

Key to the success of these optical interconnects is the high-performance and ruggedization of the electro-optic modulator (EOM), typically implemented either as a remoted external device or as a directly modulated light source. This PhD dissertation addresses the challenges of optical interconnects for harsh environments in the following manner: (1) a novel and wavelength division multiplexed (WDM) scalable optical interconnect architecture has been developed—whereby the remoted EOM has been

implemented as a microring resonator—and reduces both system complexity and energy consumption, (2) a high-speed optical link operating at cryogenic temperatures has been demonstrated—utilizing a silicon photonic based EOM—in addition to laser wavelength locking of the microring resonator, and (3) a semiconductor physics based model of the EOM has been developed to address the temperature dependent effects of the silicon p-n junction embedded in the microring resonator—based on the free-carrier plasma dispersion effect in doped silicon—to aid in the device design and optical interconnect link optimization for various harsh environment applications. Lastly, an outlook and suggested areas for future research—in the area of optimized silicon photonic devices for harsh environments—is given.

TABLE OF CONTENTS

LIST OF FIGURES

Chapter 1 – INTRODUCTION

This chapter is based in part on the work in [1].

The field of photonics has witnessed substantial growth in the past decade, primarily attributed to advances in datacenter and long-haul transceivers [2]. Growing data demands within and among datacenters – and for 5G/6G communications – has led to the development of high-speed (100 Gbps) and low-cost silicon photonics-based transceivers. The technology and intellectual property (IP) developed for these applications is then often used for optical interconnects (OI), where small-form factor and high reliability generally outweigh single channel performance as they are used for much shorter links (e.g., chip-to-chip or board-to-board). Silicon photonics is often viewed as the preferred platform to realize high-performance transmitter and receiver devices for both transceivers and optical interconnects, due to the maturation of complementary metal-oxide-semiconductor (CMOS) foundry processes, development of ever smaller technology nodes, low-cost manufacturing at high volumes, and monolithic integration with electronic integrated circuit devices [3]. Recent demonstrations of silicon photonic based optical interconnects for chip-to-chip communication have shown that >1 Tbps is possible by leveraging wavelength division multiplexing (WDM) techniques [4].

1.1. Historical Perspective

Early concentrated developments in optical interconnects, starting around 1985, targeted both inter- and intra-chip digital communications for computing purposes (see Figure 1.1). While semiconductor and dielectric waveguide technology was still immature, many of the OI architectures envisioned the use of free-space optic (FSO) links, making use of well-established laser and photodetector devices that would be hybrid integrated. From 1990 to 2000, the field witnessed the rise of photonic integrated circuits (PIC) for inter- and intra-chip optical interconnects, and for digital applications such as fiber-to-the-home (FTTH), local area networks (LAN) and wide area networks (WAN). From 2000 to 2010, research in achieving Tbps aggregate data rates via WDM gained prominence, for optical backplane and board-to-board OI, in addition to long-haul links. The 20-year time period also witnessed the first attempts at OIs for cryogenic and high-radiation environments, primarily driven by applications in aerospace. From 2010 to 2020, much of the focus in OI was on transceivers for datacenters, as various entertainment and social media platforms dominated the information content, and further progress was made in OI for harsh environment applications, within the defense and energy sectors. Beyond 2020, OI will continue to see increased development for harsh environment application in defense and commercial areas.

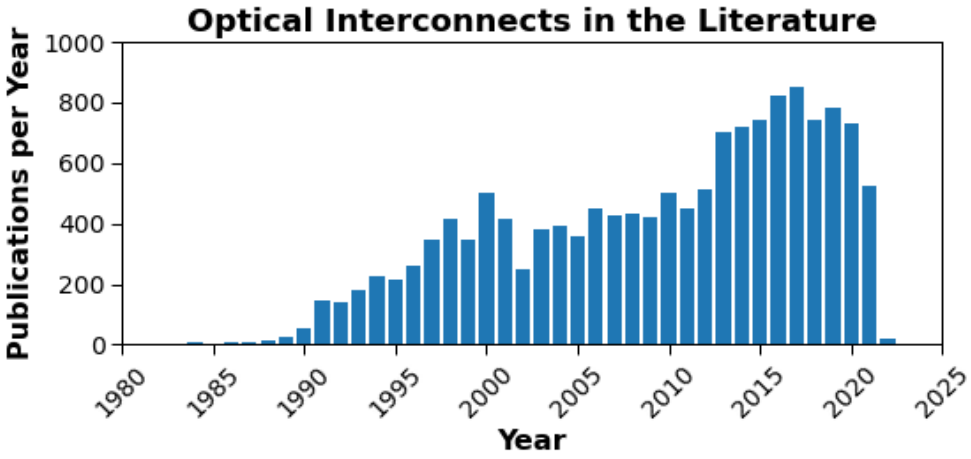

Figure 1.1: Publications per year from 1980 to 2022, pertaining to optical interconnects. Prior to 1980, publication rates were ~1 per year. Substantial growth is seen around 1990 up through the "dot com" years with a cooling off period thereafter. Accelerated growth resumes around 2013 until the present, with slight decreases in 2020 to 2022 likely attributed to the COVID-19 global pandemic. Source: Clarivate Web of Science. Date queried: 1/11/2022. Image from [1].

1.2. Application and Platform Perspective

While recent developments in optical interconnects have demonstrated substantial potential to address growing data demands, these have primarily been designed to operate in relatively benign and controlled environments. As the complexity and size of both classical and quantum based electronic systems grow, there is an emerging need to utilize an optical interconnect to facilitate high aggregate data ingress and egress. Furthermore, these advanced electronic systems are often employed in harsh environments, either to enable high performance (as in superconducting electronics) or as a result of the application (e.g., satellites in low-earth orbit). Silicon photonics technology that has been developed for datacenter applications is not likely to be directly inserted into harsh environments, as there are significant challenges that must be addressed, from the device physics, to the packaging, all the way up to the link level. However, the growing communications needs within harsh

environments can leverage the technology originally developed for datacenters as a starting point, as there is significant overlap (see Figure 1.2). As mentioned, small form-factor and high reliability are primary concerns, however energy consumption is also a critical concern, especially for cryogenic applications or where many such interconnects are needed. In this paper, the primary focus will be on optical interconnects used in cryogenic and high-radiation environments, as these represent many of the current and emerging needs, and address design issues at all levels of the optical interconnect.

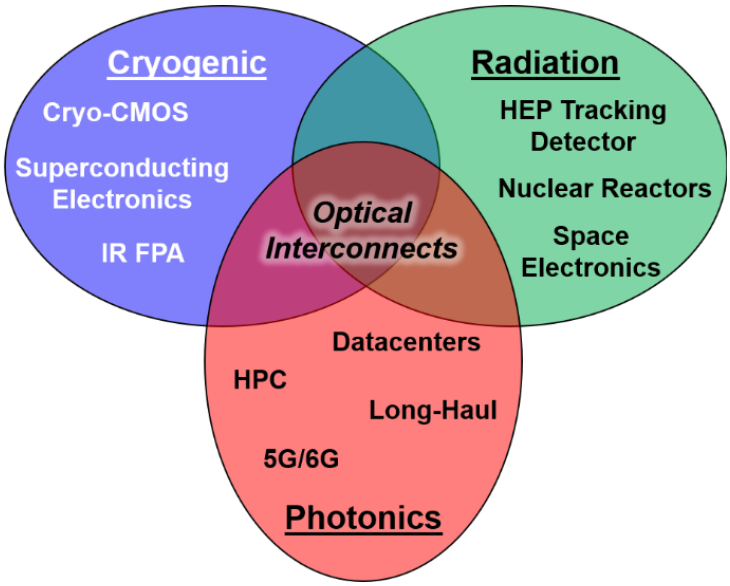

Figure 1.2: Application areas for devices operating in cryogenic and high radiation harsh environments, along with the overlap of applications for photonics. Image from [1].

Chapter 2 – TEMPERATURE DEPENDENT SEMICONDUCTOR DEVICE PHYSICS

2.1. Introduction to Silicon

Silicon (Si) is a material element found within the Group IV of the Periodic Table of Elements and is the cornerstone of modern electronics based on complimentary metal-oxide-semiconductor (CMOS) technology and fabrication processes, which is a critical enabler for present and future silicon photonics [5]. Silicon has a diamond crystal lattice, and is non-centrosymmetric due to the offset face-centered crystal (FCC) structure (see Figure 2.1), and is an indirect bandgap material ($E_g \approx 1.11$ eV at 300 K and 1.17 eV at 0 K) due to the reciprocal lattice of the diamond crystal structure [6]. The material properties of Si determine the electrical, thermal, and mechanical responses, enabling various electro-optic phenomena.

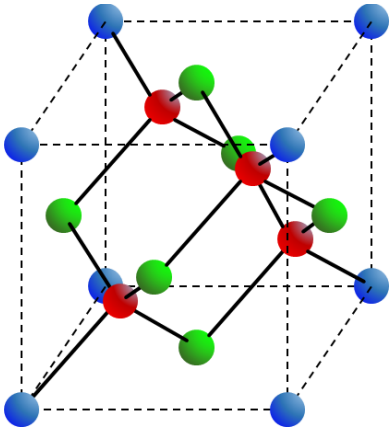

Figure 2.1: Primitive unit cell for the diamond crystal lattice of Si. Blue atoms correspond to BCC lattice, blue and green atoms correspond to FCC, and the red atoms correspond to the $\left(\frac{1}{4},\frac{1}{4},\frac{1}{4}\right)$ offset FCC atoms.

2.2. Fermi-Dirac and Maxwell-Boltzmann Statistics

The probability or occupancy of a Fermion (e.g., an electron) being excited from the valence band to the conduction band is related to its energy E and governed by a distribution function $f(E)$. The Fermi-Dirac distribution is expressed as:

$$f(E) = \frac{1}{1 + \exp\left(\frac{E - E_F}{k_B T}\right)} \tag{2-1}$$

where E_F is the Fermi energy, k_B is the Boltzmann constant, and T is the temperature [6]. In the case where $E - E_F \gg k_B T$, then the function $f(E) \to 0$. In the other case where $E - E_F \ll k_B T$, then the function $f(E) \to 1$. Additionally, when $E = E_F$, then $f(E) = 0.5$.

Particle energy distributions can also be expressed by Maxwell-Boltzmann statistics as [7]:

$$f(E) = \exp\left(-\frac{E - E_F}{k_B T}\right)$$

$$= \exp\left(\frac{E_F - E}{k_B T}\right) \tag{2-2}$$

Note that when $E - E_F \gg k_B T$, then the function $f(E) \to 0$, which is the same distribution behavior as the for the Fermi-Dirac variant. Thus, as can be seen in [7] and Figure 2.2, as the absolute energy difference $|E - E_F|$ increases the Maxwell-Boltzmann distribution function approaches the Fermi-Dirac function.

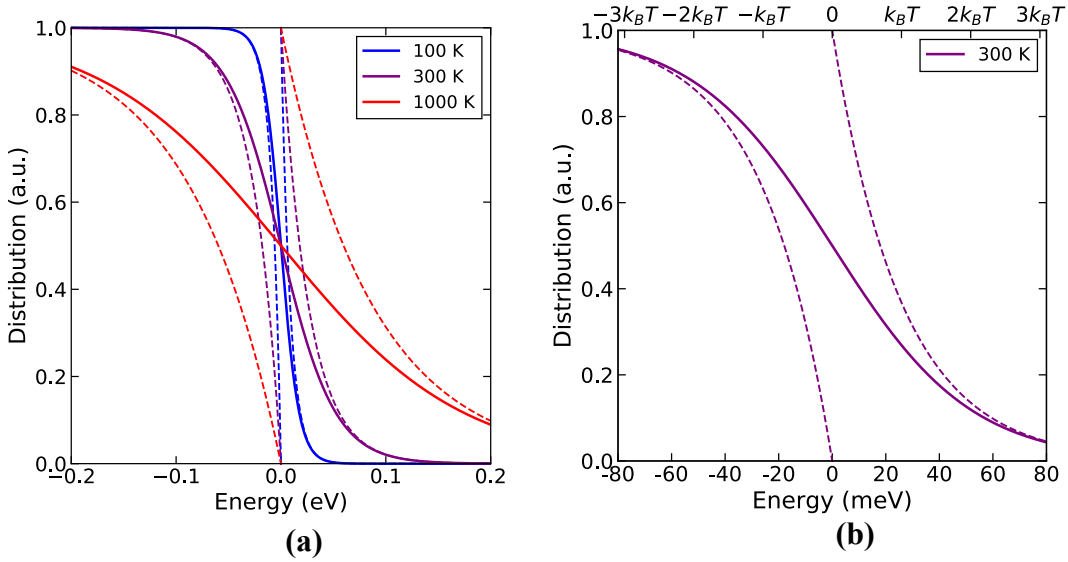

Figure 2.2: (a) Fermi-Dirac (solid lines) and Maxwell-Boltzmann (dashed lines) distributions as a function of energy for temperatures at 100 K, 300 K, and 1000 K. (b) Fermi-Dirac (solid line) and Maxwell-Boltzmann (dashed line) distributions as a function of energy at 300 K.

2.3. Energy Bandgap

The energy bandgap of semiconductors always diminishes when its temperature is increased [8], [9]. This is due to an increase in the effective interatomic spacing as determined by the crystal lattice, which reduces the potential energy as seen by the bound electrons in the host atoms.

A semi-empirical relationship to describe the temperature (T) dependence of the energy gap (E_g), known as the Varshni model, is given as:

$$E_g(T) = E_g(0) - \frac{\alpha T^2}{T + \beta}, \tag{2-3}$$

where $E_g(0)$ (eV), α (eV K^{-1}) and β (K) are the fitting coefficients of the model [9]. Note that $E_g(0)$ is the bandgap at temperature 0 K. The Varshini fitting parameters for Ge and Si are given in Table 2.1.

Table 2.1: Varshni fitting parameters.

Material	$E_g(0)$ (eV)	α (eV K^{-1})	β (K)
Germanium	0.7437	4.774 x 10^{-4}	235
Silicon	1.1695	4.73 x 10^{-4}	636

A more precise assessment of the bandgap energy between 2 K and 300 K is given by the Bludau model [10], and is described as:

$$E_g(T) = A + BT + CT^2. \tag{2-4}$$

The coefficients of the Bludau model for Si are given in Table 2.2, and are broken up according to two temperature regimes, one from $0 < T \leq 190$ K and the other from $150 \leq T \leq 300$ K.

Coefficient	$0 \leq T \leq 190$ K	$150 \leq T \leq 300$ K
A (eV)	1.170	1.1785
B (eV K^{-1})	1.059	-9.025
C (eV K^{-2})	-6.05 x 10^{-7}	-3.05 x 10^{-7}

Table 2.2: Bludau et al model coefficients for Si

The calculated bandgap energy of Si as a function of temperature, assuming the Varshni and Bludau models, are shown together in Figure 2.3.

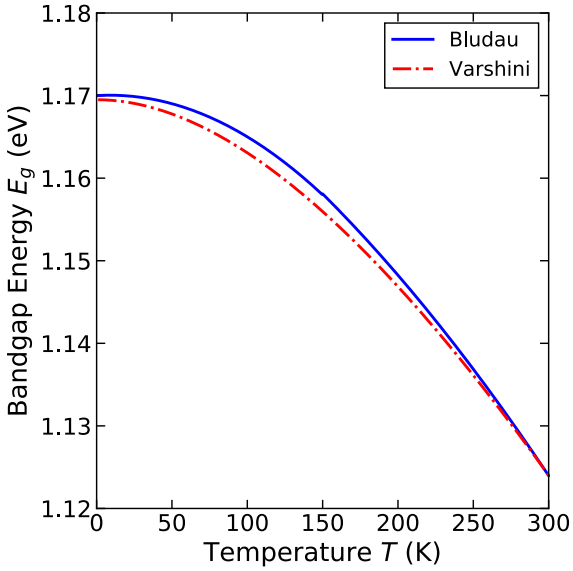

Figure 2.3: Bandgap energy of intrinsic Si as a function of temperature, assuming the Bludau model (solid line) and Varshni model (dot-dash line).

2.4. Temperature Dependent Density-of-States Effective Mass

The density-of-states (DOS) effective mass is also dependent on the crystal lattice temperature. The DOS effective mass is a scalar value that encapsulates non-idealities of an energy band, including degeneracy and non-spherical energy surfaces distributed non-parabolically in k-space [11]. The effective mass is expected to change as a function of temperature due to three primary mechanisms:

1) The change of lattice spacing with temperature
2) The temperature change of the Fermi-distribution function in a non-parabolic band
3) The explicit temperature variation of the band curvature due to the interaction between electrons and phonons

In the conduction band minima of Si there exists an ellipsoidal constant energy surface, characterized by both longitudinal and transverse effective masses, where $m_\ell^* = m_\ell/m_0$ and

$m_t^* = m_t/m_0$, respectively and shown in Figure 2.4. For an ellipsoidal band, the DOS effective mass is defined as the geometric mean over three axis and considering the band degeneracy, given as:

$$m_e^* = (g_V)^{2/3}(m_\ell^* m_t^{*2})^{1/3},$$

(2-5)

where g_V is the degeneracy level. For Si, there exists 6 conduction band minima and hence, $g_V = 6$.

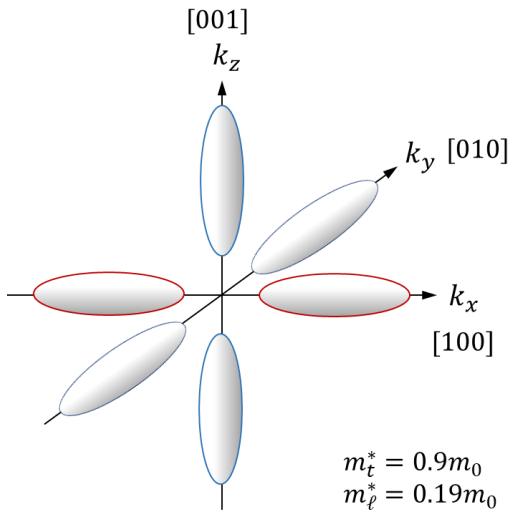

Figure 2.4: Constant energy ellipsoids for the conduction band of Si, corresponding to the 6 conduction band minima, where $\boldsymbol{m_\ell^*}$ and $\boldsymbol{m_t^*}$ and the longitudinal and transverse effective mass, respectively. Image recreated based on [6], [7].

A simplified expression for temperature dependent DOS effective mass has been reported as [12]:

$$m_e^* = m_0(A + BT + CT^2 + DT^3)$$

(2-6)

$$m_h^* = m_0(A + BT + CT^2 + DT^3 + ET^4),$$

(2-7)

with the coeffiecents for each expression given in Table 2.3.

Coefficient	m_e^*	m_h^*
A	1.057	0.584
B	2.862 x 10^{-4}	2.712 x 10^{-4}
C	7.580 x 10^{-7}	5.857 x 10^{-6}
D	-1.084 x 10^{-9}	-1.969 x 10^{-8}
E	-	1.872 x 10^{-11}

Table 2.3: Temperature coefficients for the DOS effective mass for electrons and holes in the conduction band of Si.

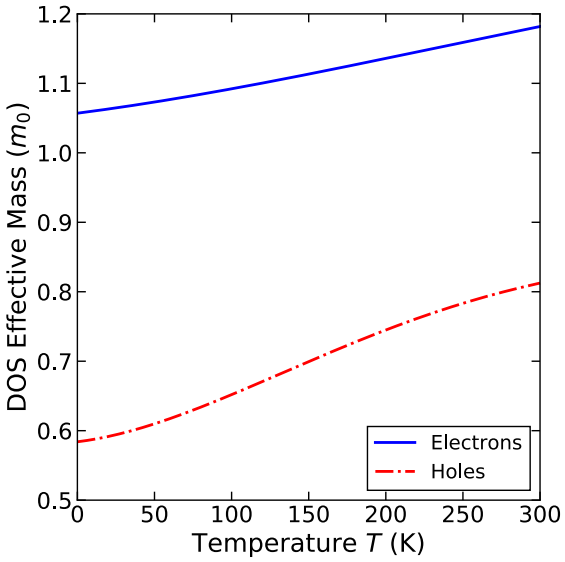

Figure 2.5: Density-of-State effective mass for both electrons and holes in Si, as a function of temperature.

2.5. Intrinsic Carrier Concentration

Under thermal equilibrium, the intrinsic carrier concentration is given as:

$$n_i = \sqrt{N_C N_V} \exp\left(-\frac{E_g}{k_B T}\right), \tag{2-8}$$

where N_C and N_V are the effective densities of states in the conduction and valence band, respectively. The effective densities of states are expressed as:

$$N_C = 2\left(\frac{2\pi m_e^* k_B T}{h^2}\right)^{1.5} \tag{2-9}$$

$$N_V = 2\left(\frac{2\pi m_h^* k_B T}{h^2}\right)^{1.5}, \tag{2-10}$$

where m_e^* and m_h^* are the effective masses of electrons and holes for density of state calculations.

By combining the temperature dependent effects of the bandgap and effective mass, the intrinsic carrier concentration can be more accurately described, as is shown in Figure 2.6. In the temperature range $0 < T \leq 300$ K, the Bludau model is used, and for $T > 300$ K, the Varshini model is used.

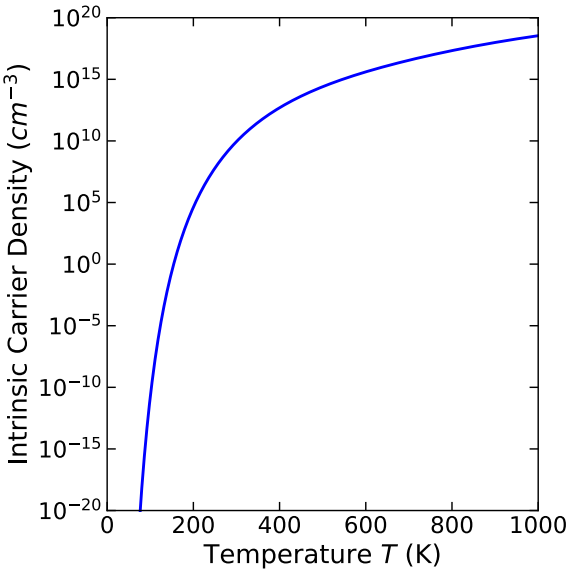

Figure 2.6: Intrinsic carrier concentration of Si as a function of temperature, including effects of changing bandgap energy and effective mass using the Bludau and Vashini models.

2.6. Extrinsic Carrier Concentration

Extrinsic semiconductors can be formed by doping the host crystal material with either donor or acceptor atoms (i.e., phosphorus or boron) to form n- or p-type semiconductors, respectively. Donor (or acceptor) atoms create useful devices at room temperature as the electrons (or holes) are considered completely thermalized at room temperatures (e.g., 300 K). At cryogenic temperatures however, the donor (or acceptors) atoms cannot be considered completely thermalized, and thus the effects of partial ionization at low temperatures must be considered.

2.6.1. Space-Charge Neutrality

First, we consider the fact that space-charge neutrality must be maintained in either a *n*- or *p*-type semiconductor material:

$$n(T) = N_D(T) - N_A(T) + \frac{n_i^2(T)}{n(T)} \tag{2-11}$$

$$p(T) = N_A(T) - N_D(T) + \frac{n_i^2(T)}{p(T)}, \tag{2-12}$$

where $n(T)$ and $p(T)$ are the majority carrier concentrations, $N_D(T)$ and $N_A(T)$ are the total neutral donor and acceptor atom concentrations, respectively.

2.6.2. Partial Ionization

The partial ionization of dopant atoms in the host crystal material is governed by Fermi-Dirac statistics, and takes the form:

$$N_D^+ = N_D \left[1 + g_{CD} \exp\left\{\left(\frac{\Delta E_D}{k_B T}\right) + \left(\frac{E_{fn} - E_C}{k_B T}\right)\right\}\right]^{-1}$$

(2-13)

$$N_A^- = N_A \left[1 + g_{VD} \exp\left\{\left(\frac{\Delta E_A}{k_B T}\right) + \left(\frac{E_{fp} - E_V}{k_B T}\right)\right\}\right]^{-1},$$

(2-14)

where $N_D^+(T)$ and $N_A^-(T)$ are the partial donor and acceptor atom concentrations, g_{CD} and g_{VD} are the conduction and valence band degeneracy level (e.g. $g_{CD} = 2$ and $g_{VD} = 4$ for typical semiconductors), ΔE_D and ΔE_A are the donor and acceptor energy level (e.g. $\Delta E_D = 46$ meV for P in Si and $\Delta E_A = 46$ meV for B in Si) , and E_{fn} and E_{fp} are the electron and hole quasi-Fermi level, respectively [13].

2.6.3. Carrier Freeze-Out

The concept of partial ionization is most readily applied to doped semiconductors at low temperatures, where they experience carrier freeze-out. In this regime, the dopants are only partially thermalized and their contribution to the free carrier concentration diminishes rapidly. As an example, consider an *n*-type semiconductor, where $N_A \sim 0$, i.e., the *p*-type doping level is negligible [14]. Re-visiting the corresponding expression (Eq. (2-11)) for charge neutrality, in this example of carrier freeze-out due to incomplete ionization, leads to the following quadratic equation:

$$n^2(T) - N_D^+ n(T) - n_i^2(T) = 0$$

(2-15)

The solutions to this equation then lead to the familiar expression:

$$n(T) = \frac{N_D^+(T)}{2} + \left[\left(\frac{N_D^+(T)}{2}\right)^2 + n_i^2(T)\right]^{1/2},$$

(2-16)

where only the positive root is considered as the non-trivial solution. Although this form is appealing, to accurately solve for the partial ionization level, the Fermi energy must be calculated from the total free carrier concentration using:

$$n = N_C \exp\left(\frac{E_{fn} - E_C}{k_B T}\right)$$

(2-17)

$$p = N_V \exp\left(\frac{E_{fp} - E_V}{k_B T}\right).$$

(2-18)

By substitution of the Fermi energy expression into the partial ionization the expression, and then back into the quadratic equation above, a cubic equation in $n(T)$ arises:

$$n(T) - \frac{A}{1 + Bn(T)} n(T) - C = 0,$$

(2-19)

where $A = N_D$, $B = \frac{g_{CD}}{N_V} \exp\left(\frac{\Delta E_D}{k_B T}\right)$, and $C = n_i^2(T)$. Simplifying the equation further, by multiplying through by the denominator $1 + Bn(T)$ and collecting the common terms, leads to the final cubic expression:

$$Bn^3(T) + n^2(T) - (A + CB)n(T) - C = 0.$$

(2-20)

Note that only a real and positive root will yield a non-trivial solution. Utilizing all the temperature dependencies formulated earlier, the majority free carrier density for *n*-type Si as a function of varying dopant concentrations, is shown in Figure 2.7.

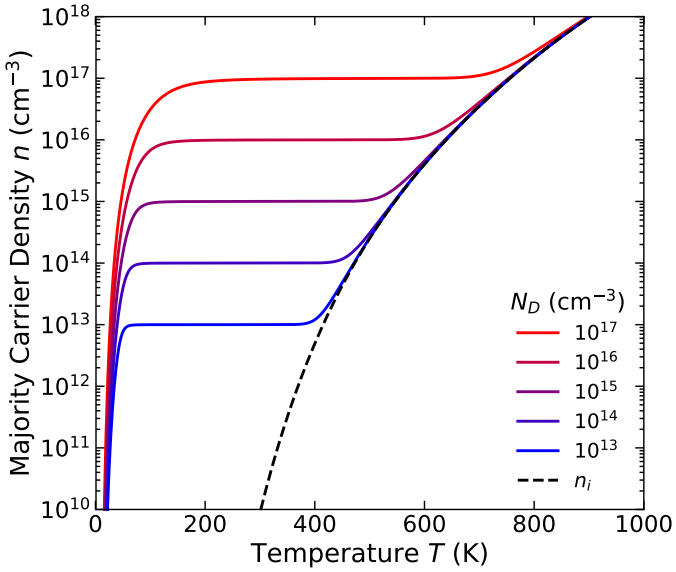

Figure 2.7: Extrinsic majority free carrier concentration of n-type Si as a function of temperature and for varying P dopant concentration levels (solid lines). The intrinsic carrier concentration (dashed line) is shown for comparison.

The point at which the free carrier concentration n drops below the dopant concentration N_D (i.e., when $n/N_D < 1$) is denoted as the carrier freeze out temperature. The relative temperature dependent changes are easier to visualize when the ratio n/N_D is plotted against the temperature, as shown in Figure 2.8. Using low to moderate doping conditions (i.e., $10^{13} - 10^{16}$ cm^{-3}) the dopant atoms are fully ionized, and hence exhausted, and behave as an extrinsic material at typical operating temperatures. An increase in dopant concentration allows the semiconductor to operate in the exhausted regime at higher temperatures, however it quickly reverts to the free carriers from the host material and appears intrinsic.

As the temperature decreases away from the region of exhaustion, the host material no longer has enough energy to thermalize all free carriers, and the carrier density behavior is governed by Fermi-Dirac statistics. Clearly, a higher doping concentration makes the device less sensitive to changes in total carrier density to temperature, as can be seen by analyzing

the slope. The temperature at which the semiconductor enters freeze-out can be more readily observed when plotted proportionally against $1/T$. Interestingly, the carrier freeze-out temperature *decreases* with increasing dopant concentration; this is true for both *p*- and *n*-type Si.

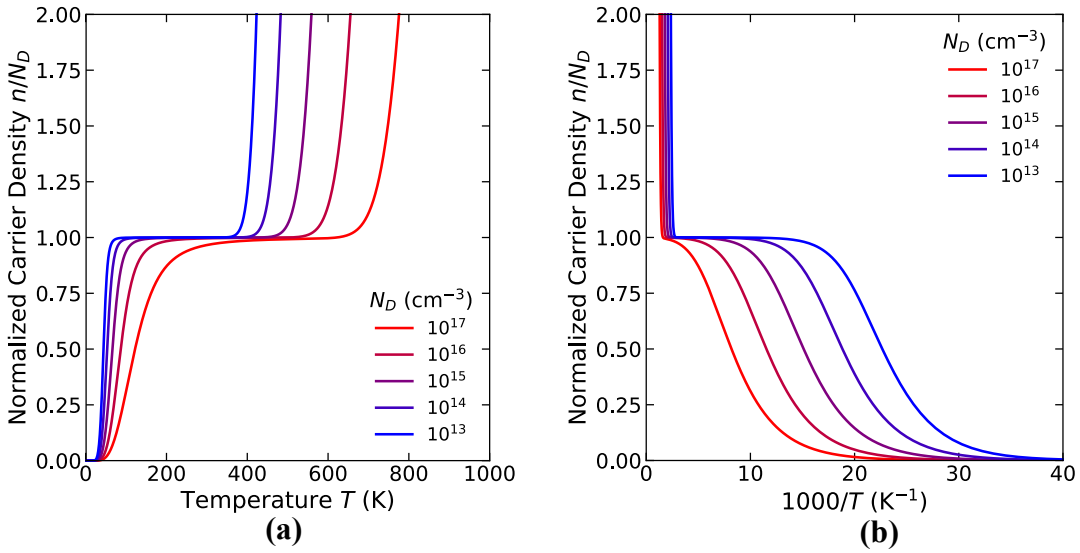

Figure 2.8: Normalized carrier density in Si as a function of (a) temperature and (b) inverse temperature for various P dopant concentrations.

2.7.Semiconductor Material Permittivity

2.7.1. Classical Electron Harmonic Oscillator Model

Assume that an electron is bound to an atomic nucleus with classical dynamics that can be described as two masses coupled via spring. Considering that the mass of nucleus (e.g., for a single Si nucleus 28.0855 u = 4.66×10^{-26} kg) is typically many orders of magnitude larger than that of a single electron (9.11×10^{-31} kg), we can assume the scenario to be that of an electron coupled via spring to an infinite mass. Thus, the system can be modeled as a second-order differential equation, with respect to position, from Newtons 2nd Law of motion:

$$m_e \frac{\partial^2 \boldsymbol{r}(t)}{\partial t} = \sum_i \boldsymbol{F}_i = \boldsymbol{F}_E(t) + \boldsymbol{F}_R(t) + \boldsymbol{F}_D(t),$$

(2-21)

where m_e is the mass of the electron and $\boldsymbol{r}(t)$ is the distance deviation from equilibrium. All forces $\boldsymbol{F}_i$ acting on the electron must be considered (hence the summation), however in this example there are three primary forces. The first, $\boldsymbol{F}_E$, is the time-dependent force applied from an external electric field of the form $\boldsymbol{F}_E(t) = q\boldsymbol{E}_0 e^{-j\omega t}$. The second, $\boldsymbol{F}_R(t)$, is the restoring force (analogous to Hooke's Law) where $\boldsymbol{F}_R(t) = -k\boldsymbol{r}(t)$ and $k = m_e\omega_0^2$. Lastly, $\boldsymbol{F}_D(t)$, the damping force is given by $\boldsymbol{F}_D(t) = -\gamma m_e \frac{\partial \boldsymbol{r}(t)}{\partial t}$ where γ is the damping constant. Inserting the expression for each force back into the main equation and rearranging leads to the following expression

$$m_e \frac{\partial^2 \boldsymbol{r}(t)}{\partial t} + \gamma m_e \frac{\partial \boldsymbol{r}(t)}{\partial t} + m_e\omega_0^2 \boldsymbol{r}(t) = q\boldsymbol{E}_0 e^{-j\omega t}.$$

(2-22)

Assuming a monochromatic plane wave is incident on the atom under consideration, and a wave-like distance deviation solution from equilibrium of the form $\boldsymbol{r} = \boldsymbol{r}_0 e^{-j\beta z} e^{-j\omega t}$ can be given as:

$$\boldsymbol{r}(\omega) = \frac{q}{m_e(\omega_0^2 - \omega^2 - j\gamma\omega)} \boldsymbol{E}(\omega).$$

(2-23)

The instantaneous polarization due to an induced dipole moment, from an ensemble of electrons with density N_e, is given as:

$$\boldsymbol{P} = N_e q \boldsymbol{r}(\omega) = \frac{N_e q^2}{m_e(\omega_0^2 - \omega^2 - j\gamma\omega)} \boldsymbol{E}(\omega).$$

(2-24)

The polarization can also be related to the applied electric field via the electron susceptibility χ_e as:

$$\boldsymbol{P} = \varepsilon_0 \chi_e \boldsymbol{E}(\omega) = \varepsilon_0(\varepsilon_r - 1)\boldsymbol{E}(\omega),$$

(2-25)

where ε_0 is the vacuum permittivity and ε_r is the relative permittivity. By comparing the above-mentioned relations, we can now the describe the frequency-dependent electron susceptibility as:

$$\chi_e = \frac{N_e q^2}{m_e \varepsilon_0(\omega_0^2 - \omega^2 - j\gamma\omega)}$$

(2-26)

Thus, the relative permittivity is described as:

$$\varepsilon_r(\omega) = 1 + \frac{\omega_p^2}{\omega_0^2 - \omega^2 - j\gamma\omega},$$

(2-27)

where $\omega_p^2 = N_e q^2 / m_e \varepsilon_0$ is the plasma frequency. The complex permittivity can now be separated into real and imaginary components $\varepsilon_r = \varepsilon' + j\varepsilon''$, by multiplying by the complex conjugate, where:

$$\varepsilon' = 1 + \frac{\omega_p^2(\omega_0^2 - \omega^2)}{(\omega_0^2 - \omega^2)^2 + \gamma^2\omega^2}$$

(2-28)

$$\varepsilon'' = \frac{\gamma\omega_p^2\omega}{(\omega_0^2 - \omega^2)^2 + \gamma^2\omega^2}.$$

(2-29)

2.7.2. Drude Model of Material Permittivity (Intra-band)

In the Drude model, we assume that the electrons are not bound to the atomic nucleus and are thus "free carriers" that move throughout the material, as in a metal or electrons in the conduction band of a semiconductor. Just as in the classical harmonic oscillator, we first consider all forces on the electron:

$$m_e \frac{\partial^2 \boldsymbol{r}(t)}{\partial t} = \boldsymbol{F}_E(t) + \boldsymbol{F}_D(t).$$

(2-30)

Notice that the restoring force $\boldsymbol{F}_R(t)$ has been removed, leading to the new equation:

$$m_e \frac{\partial^2 \boldsymbol{r}(t)}{\partial t} + \gamma m_e \frac{\partial \boldsymbol{r}(t)}{\partial t} = q\boldsymbol{E}_0 e^{-j\omega t}.$$

(2-31)

The solution to the motion of a free electron can be expressed as:

$$\boldsymbol{r}(\omega) = -\frac{q}{m_e(\omega^2 + j\gamma\omega)}\boldsymbol{E}(\omega)$$

(2-32)

The instantaneous polarization due to an induced dipole moment, from an ensemble of electrons with density N_e, is given as:

$$\boldsymbol{P} = N_e q\boldsymbol{r}(\omega) = -\frac{N_e q^2}{m_e(\omega^2 + j\gamma\omega)}\boldsymbol{E}(\omega).$$

(2-33)

The polarization can also be related to the applied electric field via the electron susceptibility χ_e as:

$$\boldsymbol{P} = \varepsilon_0 \chi_e \boldsymbol{E}(\omega) = \varepsilon_0(\varepsilon_r - 1)\boldsymbol{E}(\omega),$$

(2-34)

where ε_0 is the vacuum permittivity, and ε_r is the relative permittivity. By comparing the above-mentioned relations, we can now the describe the frequency-dependent electron susceptibility as:

$$\chi_e = -\frac{N_e q^2}{m_e \varepsilon_0 (\omega^2 + j\gamma\omega)} \tag{2-35}$$

Thus, the relative permittivity is described as:

$$\varepsilon_r(\omega) = 1 - \frac{\omega_p^2}{\omega^2 + j\gamma\omega}, \tag{2-36}$$

where $\omega_p^2 = N_e q^2 / m_e \varepsilon_0$ is the plasma frequency. The complex permittivity can now be separated into real and imaginary components $\varepsilon_r = \varepsilon' + j\varepsilon''$, by multiplying by the complex conjugate, where:

$$\varepsilon' = 1 - \frac{\omega_p^2}{\omega^2 + \gamma^2} \tag{2-37}$$

$$\varepsilon'' = \frac{\gamma\omega_p^2}{\omega(\omega^2 + \gamma^2)} \tag{2-38}$$

An example simulation of the Drude model is shown in Figure 2.9(a).

2.7.3. Lorentz Model of Material Permittivity (Inter-band)

The Lorentz model is similar in formulation to that of the classical electron harmonic oscillator. Here, electron resonances due to high-energy interband transitions are assumed to order to corroborate with experimental measurements. In the Lorentz oscillator model, we assume a superposition of oscillators:

$$\varepsilon_r(\omega) = 1 + \sum_i^k \frac{c_i \omega_i^2}{\omega_i^2 - \omega^2 - j\gamma_i \omega},$$

(2-39)

where ω_i is the i[th] resonance frequency, c_i is a resonance amplitude coefficient, and γ_i is the i[th] damping coefficient. An example simulation of the Lorentz model is shown in Figure 2.9(b).

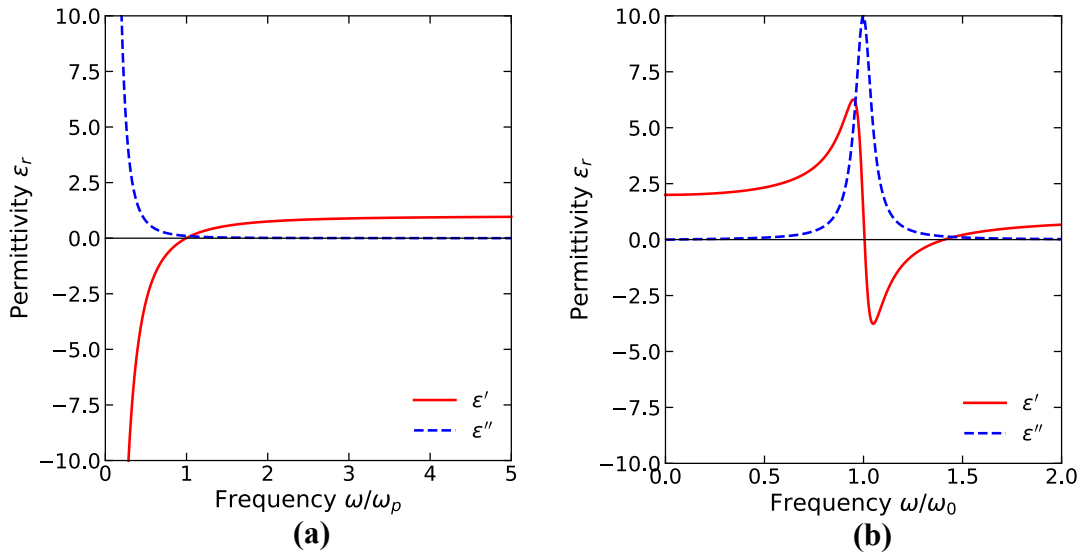

Figure 2.9: Complex permittivity as a function of frequency for (a) Drude model, with $\boldsymbol{\gamma = 0.1}$ and (b) Lorentz model for a single oscillator, with $\boldsymbol{c_1 = \omega_1 = 1}$ and $\boldsymbol{\gamma_1 = 0.1}$.

2.7.4. Drude-Lorentz Model

To better match the experimental response of semiconductor materials, the Drude-Lorentz model is used, which combines the models produced by Drude and Lorentz that describe optical responses due to intra- and inter-band electron transitions, respectively (see Figure 2.10).

$$\varepsilon_r(\omega) = 1 - \frac{\omega_p^2}{\omega^2 + j\gamma_d\omega} + \sum_i^k \frac{c_i\omega_i^2}{\omega_i^2 - \omega^2 - j\gamma_i\omega}, \tag{2-40}$$

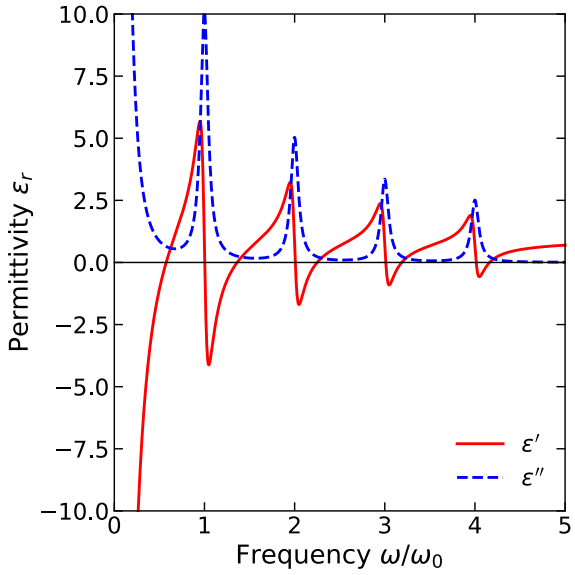

Figure 2.10: Drude-Lorentz model with four oscillators at $\boldsymbol{\omega_0 = 1, 2, 3}$ & $\boldsymbol{4}$, and with $\boldsymbol{c_1 = \omega_1 = 1}$ and $\boldsymbol{\gamma = \gamma_1 = 0.1}$.

2.7.5. Free-Carrier Plasma Dispersion

Although carrier freeze-out in semiconductor devices presents a limit in performance at low temperatures, the relevant operating principles of the modulator must be considered. Most high-speed semiconductor devices are comprised of a *p-n* or *p-i-n* junction, where carrier transit-time and electrical parasitics dominate the response. Due to the presence of a junction capacitance, a reverse bias voltage is often applied to widen the junction and reduce the associated capacitance to increase the RC-limited bandwidth. The process of carrier depletion can be utilized to change the refractive index, causing a change in the phase of a propagating electric field, which is known as the plasma dispersion effect.

The plasma dispersion effect can be approximated using a Drude model, where the operating frequency ω is assumed to be well away from the resonant frequency ω_0. Thus, this scenario is equivalent to considering only intra-band electron-hole transitions, and not inter-band (i.e., absorption or emission across the bandgap). One can easily see in Figure 2.11, that the Drude model approximates the Lorentz model when $\omega \gg \omega_0$, also implying that the carriers are free (as in a doped semiconductor at room temperature) and not bound to the host atom nucleus.

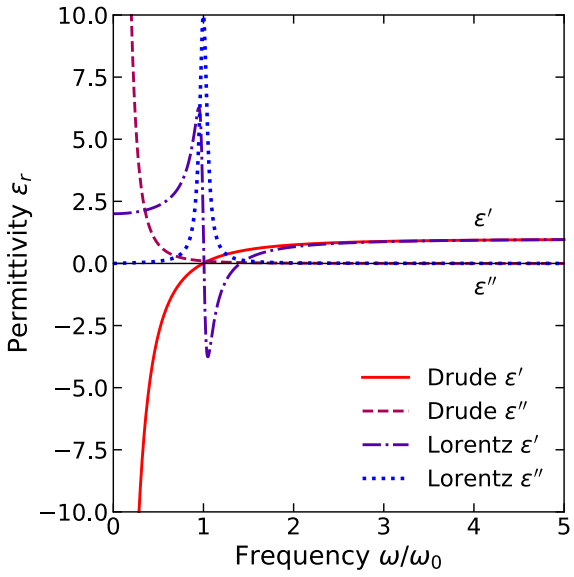

Figure 2.11: Comparison between the Drude and Lorentz permittivity material models, where the two are approximately the same for $\boldsymbol{\omega \gg \omega_0}$. Parameters used are $\boldsymbol{\gamma = 0.1}$, $\boldsymbol{c_1 = \omega_1 = 1}$ and $\boldsymbol{\gamma_1 = 0.1}$.

Starting with the complex relative permittivity derived earlier in Eq. (2-36):

$$\varepsilon_r(\omega) = 1 - \frac{\omega_p^2}{\omega^2 + j\gamma\omega},$$

(2-41)

where $\omega_p^2 = N_e q^2/m_e\varepsilon_0$ is the electron plasma frequency. Note that in the case of a doped semiconductor, we must consider the plasma frequency of free electrons and holes, therefore the plasma frequency can be modified as:

$$\omega_p^2 = \frac{q^2}{\varepsilon_0}\left(\frac{N_e}{m_e} + \frac{N_h}{m_h}\right)$$

(2-42)

Remembering that the complex permittivity $\varepsilon_r = \varepsilon' + j\varepsilon''$ is expressed as:

$$\varepsilon' = 1 - \frac{\omega_p^2}{\omega^2 + \gamma^2}$$

(2-43)

$$\varepsilon'' = \frac{\gamma\omega_p^2}{\omega(\omega^2 + \gamma^2)}$$

(2-44)

First, we assume that the damping coefficient γ is quite small relative to the operating frequency ω, i.e., $\omega^2 \gg \gamma^2$ which leads to:

$$\varepsilon' \approx 1 - \frac{\omega_p^2}{\omega^2}$$

(2-45)

$$\varepsilon'' \approx \frac{\gamma\omega_p^2}{\omega^3}$$

(2-46)

Next, from Maxwell's equations (specifically, Ampere-Maxwell's Law), we note the relation between a spatially varying magnetic field intensity and summation of time-dependent electric flux density and current density, which can be related back to the electric field:

$$\nabla \times \boldsymbol{H} = \frac{\partial}{\partial t}\boldsymbol{D} + \boldsymbol{J}$$

$$= \frac{\partial}{\partial t}\varepsilon\boldsymbol{E} + \sigma\boldsymbol{E}$$

(2-47)

Note that if we assume a time-harmonic field solution of the form $\boldsymbol{E} = E(x, y, z)e^{j\omega t}$, the phasor form of Ampere-Maxwell's Law becomes:

$$\nabla \times \boldsymbol{H} = \omega\varepsilon\boldsymbol{E} + \sigma\boldsymbol{E},$$

(2-48)

which leads to the relation between the current density and electric field as $\boldsymbol{J} = \sigma\boldsymbol{E}$. The current density can also be expressed as a moving charge density, i.e.:

$$\boldsymbol{J} = -qN\boldsymbol{v},$$

(2-49)

where N (cm^{-3}) is the charge density and $\boldsymbol{v}$ is the charge velocity. In a doped semiconductor, under an applied electric field $\vec{E}$, the charge velocity is equal the drift velocity where $\boldsymbol{v_d} = -q\tau/m_c^*\,\boldsymbol{E}$ where m_c^* is the conductivity effective mass and τ is the average collision time. The current density is then expressed as:

$$\boldsymbol{J} = q^2\frac{N\tau}{m_c^*}\boldsymbol{E}$$

(2-50)

The conductivity in a doped semiconductor can be re-expressed also related to the carrier mobility μ as:

$$\sigma = q^2\left(\frac{N_e\tau_e}{m_{ce}^*} + \frac{N_h\tau_h}{m_{ch}^*}\right)$$

$$= q(\mu_e N_e + \mu_h N_h)$$

(2-51)

From these relations we can see that the average collision times can be related to the conductivity mass and mobility, expressed as:

$$\tau_e^{-1} = \frac{q}{\mu_e m_{ce}^*}$$

(2-52)

$$\tau_h^{-1} = \frac{q}{\mu_h m_{ch}^*}$$

(2-53)

Next, consider that the damping coefficient γ (s^{-1}) and average collision time τ (s) are equivalent, i.e.:

$$\gamma = \tau^{-1} = \tau_e^{-1} + \tau_h^{-1} = q\left(\frac{1}{\mu_e m_{ce}^*} + \frac{1}{\mu_h m_{ch}^*}\right)$$

(2-54)

Inserting the revised relations for the plasma frequency ω_p and damping coefficient γ back into the revised Drude model for permittivity, and grouping carrier terms together leads to:

$$\varepsilon'(\omega) = 1 - \frac{q^2}{\omega^2 \varepsilon_0}\left(\frac{N_e}{m_{ce}^*} + \frac{N_h}{m_{ch}^*}\right)$$

(2-55)

$$\varepsilon''(\omega) = \frac{q^3}{\omega^3 \varepsilon_0}\left(\frac{N_e}{\mu_e {m_{ce}^*}^2} + \frac{N_h}{\mu_h {m_{ch}^*}^2}\right)$$

(2-56)

Note that the above expressions are in terms of frequency ω, which is not that useful for photonic design / simulation and generating an intuition at relevant telecommunication and data-communication wavelengths (i.e., 1.55 μm and 1.3 μm). Using the typical relations of $c = \lambda f$ and $\omega = 2\pi f$, we can substitute $\omega = \frac{2\pi}{\lambda} c$ back into the expressions:

$$\varepsilon'(\lambda) = 1 - \frac{q^2 \lambda^2}{4\pi^2 c^2 \varepsilon_0}\left(\frac{N_e}{m_{ce}^*} + \frac{N_h}{m_{ch}^*}\right)$$

(2-57)

$$\varepsilon''(\lambda) = \frac{q^3 \lambda^3}{8\pi^3 c^3 \varepsilon_0}\left(\frac{N_e}{\mu_e {m_{ce}^*}^2} + \frac{N_h}{\mu_h {m_{ch}^*}^2}\right)$$

(2-58)

Again, we typically don't deal directly with complex permittivity ε_r in photonics, and instead utilize complex refractive index $\tilde{n}$. We first note that $\tilde{n} = \sqrt{\varepsilon_r}$. Next, we can define the complex permittivity as $\tilde{n} = n' - jn''$ and let $n = n'$ and $k = n''$. Then we see that:

$$\tilde{n}^2 = (n - jk)^2 = n^2 - j2nk - k^2$$

(2-59)

Which leads to the relationship between complex permittivity and refractive index:

$$\varepsilon_r = (n^2 - k^2) - j2nk$$

(2-60)

$$\varepsilon' = n^2 - k^2$$

(2-61)

$$\varepsilon'' = 2nk$$

(2-62)

To obtain a more straightforward form of the above equations, we can use the following relation:

$$\varepsilon'^2 + \varepsilon''^2 = (n^2 - k^2)^2 + (2nk)^2 = (n^2 + k^2)^2$$

(2-63)

Combining the above relation with the expressions of complex refractive index leads to:

$$n = \frac{1}{\sqrt{2}}\left[\left[\varepsilon'^2 + \varepsilon''^2\right]^{1/2} + \varepsilon'\right]^{1/2}$$

(2-64)

$$k = \frac{1}{\sqrt{2}}\left[\left[\varepsilon'^2 + \varepsilon''^2\right]^{1/2} - \varepsilon'\right]^{1/2}$$

(2-65)

Remembering that $\tilde{n}^2 = \varepsilon_r$, the expressions for $\varepsilon_r(\lambda)$ can be simplified assuming $\omega \gg \omega_p$ and using the linear approximation $(1 - x)^r \approx 1 - rx$, thus:

$$n(\lambda) = 1 - \frac{q^2\lambda^2}{8\pi^2 c^2 \varepsilon_0}\left(\frac{N_e}{m_{ce}^*} + \frac{N_h}{m_{ch}^*}\right)$$

(2-66)

$$k(\lambda) = \frac{q^3\lambda^3}{16\pi^3 c^3 \varepsilon_0}\left(\frac{N_e}{\mu_e {m_{ce}^*}^2} + \frac{N_h}{\mu_h {m_{ch}^*}^2}\right) \tag{2-67}$$

Next, we note the relation $\alpha = 4\pi k/\lambda$ from the Beer-Lambert law, and the result is:

$$n(\lambda) = 1 - \frac{q^2\lambda^2}{8\pi^2 c^2 \varepsilon_0}\left(\frac{N_e}{m_{ce}^*} + \frac{N_h}{m_{ch}^*}\right) \tag{2-68}$$

$$\alpha(\lambda) = \frac{q^3\lambda^2}{4\pi^2 c^3 \varepsilon_0}\left(\frac{N_e}{\mu_e {m_{ce}^*}^2} + \frac{N_h}{\mu_h {m_{ch}^*}^2}\right) \tag{2-69}$$

Finally, if we solve for $\left.\frac{dn}{dN}\right|_n$ and $\left.\frac{d\alpha}{dN}\right|_n$, this yields the change in refractive index Δn and change in absorption $\Delta\alpha$ [15] that we seek:

$$\Delta n = -\frac{q^2\lambda_0^2}{8\pi^2 c^2 \varepsilon_0 n}\left(\frac{\Delta N_e}{m_{ce}^*} + \frac{\Delta N_h}{m_{ch}^*}\right) \tag{2-70}$$

$$\Delta\alpha = \frac{q^3\lambda_0^2}{4\pi^2 c^3 \varepsilon_0 n}\left(\frac{\Delta N_e}{\mu_e {m_{ce}^*}^2} + \frac{\Delta N_h}{\mu_h {m_{ch}^*}^2}\right) \tag{2-71}$$

where λ_0 is the vacuum wavelength, and ΔN_e and ΔN_h are the change in electron and hole concentrations, respectively. Although temperature is not explicitly contained in the above equations, the conductivity effective mass, mobility and refractive index are all temperature dependent.

2.8. P-N Junction

The electro-optic modulator (EOM) used in this work is based on a lateral p-n junction diode, which can be notionally described by the ideal Shockley equation [16]:

$$J = J_s\left(e^{q(V-V_j)/kT} - 1\right),$$

(2-72)

where J_s is the saturation current density, q is the electron charge, k is the Boltzmann constant, T is the temperature, V is the applied voltage, and the built-in junction voltage is given by:

$$V_j = \left(\frac{k_B T}{q}\right) \ln\left(\frac{N_A N_D}{n_i^2}\right).$$

(2-73)

From the two equations above, a strong temperature dependency exits, which is also supported by the previous derivations of Si material parameters and temperature dependences. Since current density is also directly related to the free-carrier concentration:

$$\boldsymbol{J} = q(\mu_e N_e + \mu_h N_h)\boldsymbol{E},$$

(2-74)

the temperature dependent performance of the lateral p-n junction – via the Soref-Bennett equations [15] – can be inferred and analyzed from temperature dependent current-voltage (I-V) response of the diode.

In Figure 2.12, the I-V response of the p-n junction within the ring resonator modulator (RRM) type EOM used in this work [22] is shown. The I-V was captured using a Keithley 2401 source-measurement unit (SMU) and was mechanically attached to the helium cryostat cold head with a metallic clamp and indium foil in between for thermal heatsinking [17]. The

I-V-T data in Figure 2.12 significantly deviates from the ideal diode (Shockley) equation, and can be modified with an ideality factor n [16], [18] as:

$$J = J_s\left(e^{q(V-V_j)/nkT} - 1\right). \tag{2-75}$$

Using the above non-ideal diode equation, a temperature dependent model was created to describe the data shown in Figure 2.12. In Figure 2.13, the data was modeled using the non-ideal diode equation, incorporating the Varshni model for the Si bandgap energy from Section 2.3. The model only uses a single ideality factor n, however it is known that a non-ideal diode response can have multiple n values due to such factors as generation-recombination, diffusion, high-level injection, series resistance, and self-heating effects [16], [18]. At low current levels (i.e., < 1 μA), and as the temperature decreases from 250 K to 50 K, the slope of the I-V curve increases indicating that $n > 1$ and recombination is dominant. At higher current levels (i.e., > 1 μA), the measured response significantly deviates from the model, which can likely be attributed to self-heating effects from series resistance. Other non-linear effects such as high-injection – whereby the majority carrier concentration has significantly increased above its equilibrium value – may be occurring at temperatures of 25 K and lower, below the carrier freeze-out temperature [19].

Depending on whether the p-n junction is operated in the forward or reverse bias regime, the lower carrier concentration due to low temperature induced partial ionization also impacts the optical absorption in the Si material of the lateral p-n junction, due to indirect transitions from free-carrier absorption (Section 2.7.5). However, the decreasing optical absorption due to direct transitions from the increasing bandgap energy with decreasing temperature should also be considered [20].

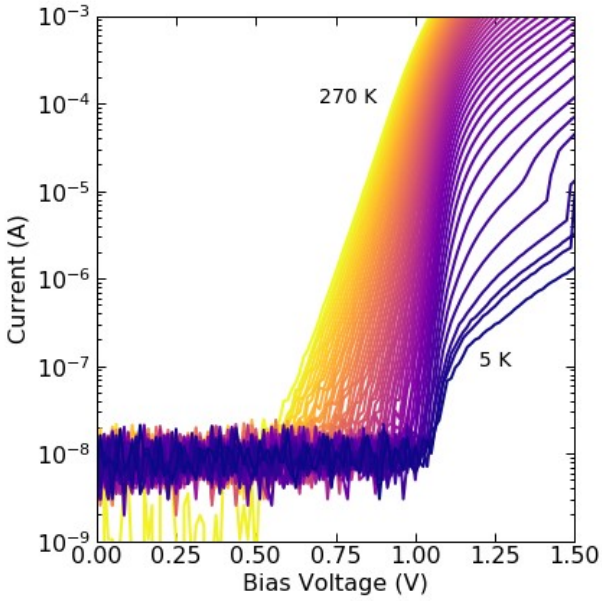

Figure 2.12: Measured temperature dependent current (A) as a function of applied bias voltage (V), from 270 K to 5 K in 5 K increments of the lateral p-n junction within the Si RRM device. Image from [22].

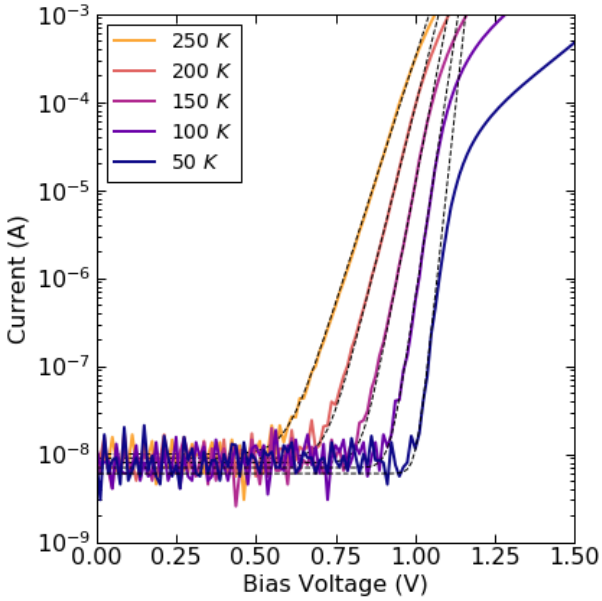

Figure 2.13: Measured (solid lines) temperature dependent current (A) as a function of applied bias voltage (V), from 250 K to 50 K in 50 K increments of the lateral p-n junction within the Si RRM device. Modeled (dashed lines) temperature dependent current (A) as a function of applied bias voltage (V), from 250 K to 50 K in 50 K increments.

Chapter 3 – MICRORING RESONATOR MODULATORS

This chapter is based in part on the work in [21] and [22].

3.1. Ring Resonators: All-Pass

In the simplest configured ring resonator, a ring waveguide is coupled to a bus waveguide by having a region of close proximity, forming a directional coupler structure. The coupling coefficient is determined by the overlap integral of evanescent fields in the lithographically defined gap region between the waveguides, and is fixed after fabrication. Since there is only one accesible output port, "all" of the light passes through, hence the name "all-pass. However, due to energy conservation, the light that resonants within the ring cavity builds up, and must be radiately dissipated. A schematic diagram of a typical all-pass ring resonator [23] is shown in Figure 3.1.

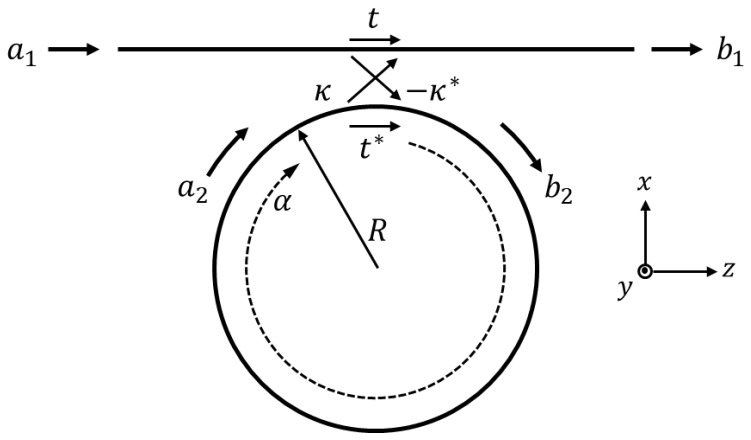

Figure 3.1: Schematic diagram of a single bus coupled "all-pass" ring resonator, whereby light is incident at port a_1, a portion of the light couples into the ring cavity at port b_2, light circulates around the cavity to port a_2, and the remaining light in the cavity along with the uncoupled light exits at port b_1.

The electric fields at each point in the ring can be described by the following equations:

$$b_1 = ta_1 + \kappa a_2 \tag{3-1}$$

$$b_2 = -\kappa^* a_1 + t^* a_2 \tag{3-2}$$

where t and κ are the complex electric field transmission and coupling coefficients, respectively. In T-matrix form [24], the electric fields in coupling region are described as:

$$\begin{bmatrix} b_1 \\ b_2 \end{bmatrix} = \begin{bmatrix} t & \kappa \\ -\kappa^* & t^* \end{bmatrix} \begin{bmatrix} a_1 \\ a_2 \end{bmatrix} \tag{3-3}$$

Note that $a_2 = \alpha e^{-j\theta} b_2$, where α is the round-trip fractional transmission (e.g. $\alpha = 1$ is lossless) and θ is the propagation phase in the ring cavity, where $\theta = \beta L_R = \left(\frac{2\pi}{\lambda} n_e\right)(2\pi R) = 4\pi^2 n_e \frac{R}{\lambda}$. Using substitution, the output of the ring is then expressed as:

$$\begin{aligned} b_1 &= ta_1 + \kappa\alpha e^{-j\theta} b_2 \rightarrow \mathbf{1^{st}\ Pass} \\ &= ta_1 + \kappa\alpha e^{-j\theta}\left(-\kappa^* a_1 + t^* \alpha e^{-j\theta} b_2\right) \rightarrow \mathbf{2^{nd}\ Pass} \\ &= ta_1 + \kappa\alpha e^{-j\theta}\left(-\kappa^* a_1 + t^* \alpha e^{-j\theta}\left(-\kappa^* a_1 + t^* \alpha e^{-j\theta} b_2\right)\right) \rightarrow \mathbf{3^{rd}\ Pass} \end{aligned} \tag{3-4}$$

Clearly the expression continues to follow a photon packet propagating around the ring. Assuming $a_1 = 1$, and further expanding the relation for b_1:

$$
\begin{aligned}
b_1 &= t + \kappa\alpha e^{-j\theta}\left(-\kappa^* + t^*\alpha e^{-j\theta}\left(-\kappa^* + t^*\alpha e^{-j\theta} b_2\right)\right) \\
&= t + \kappa\alpha e^{-j\theta}\left(-\kappa^* - \kappa^* t^*\alpha e^{-j\theta} + t^2\alpha^2 e^{-2j\theta} b_2\right) \\
&= t + \left(-\kappa^*\kappa\alpha e^{-j\theta} - \kappa^*\kappa t^*\alpha^2 e^{-2j\theta} + \kappa t^2\alpha^3 e^{-3j\theta} b_2\right) \\
&= t - \kappa^2\alpha e^{-j\theta} - t^*\kappa^2\alpha^2 e^{-2j\theta} + t^2\kappa^2\alpha^3 e^{-3j\theta} b_2 \ldots
\end{aligned}
$$

(3-5)

The expression for the output b_1 resembles the sum of an infinite geometric sequence (when a negative sign and κ^2 is factored out in the last expression above) whereby:

$$
S_\infty = \sum_{n=1}^{\infty} u^{n-1} w^n = \frac{w}{1 - uw}
$$

(3-6)

If $u = t^*$ and $w = \alpha e^{-j\theta}$, then

$$
\begin{aligned}
b_1 &= t - \kappa^2\left(\frac{\alpha e^{-j\theta}}{1 - t^*\alpha e^{-j\theta}}\right) \\
&= t\left(\frac{1 - t^*\alpha e^{-j\theta}}{1 - t^*\alpha e^{-j\theta}}\right) - \left(\frac{\kappa^2\alpha e^{-j\theta}}{1 - t^*\alpha e^{-j\theta}}\right) \\
&= \frac{t\left(1 - t^*\alpha e^{-j\theta}\right) - \kappa^2\alpha e^{-j\theta}}{1 - t^*\alpha e^{-j\theta}} \\
&= \frac{t - t^* t\alpha e^{-j\theta} - \kappa^2\alpha e^{-j\theta}}{1 - t^*\alpha e^{-j\theta}} \\
&= \frac{t - \alpha e^{-j\theta}}{1 - t^*\alpha e^{-j\theta}}
\end{aligned}
$$

(3-7)

Note that $t^2 + \kappa^2 = 1$. The complex transmission coefficient can be defined as $t = |t|e^{-j\phi}$, where ϕ is the phase shift associated with the waveguide coupling, as found through coupled-mode thoery [25].

The intensity at the output port is then given as:

$$|b_1|^2 = \left| \frac{|t|e^{-j\phi} - \alpha e^{-j\theta}}{1 - |t|e^{+j\phi}\alpha e^{-j\theta}} \right|^2$$

$$= \frac{\alpha^2 + |t|^2 - 2\alpha|t|\cos(\theta + \phi)}{1 + \alpha^2|t|^2 - 2\alpha|t|\cos(\theta + \phi)}$$

(3-8)

The wavelength dependent output is shown in Figure 3.2, in linear and logarithmic scale.

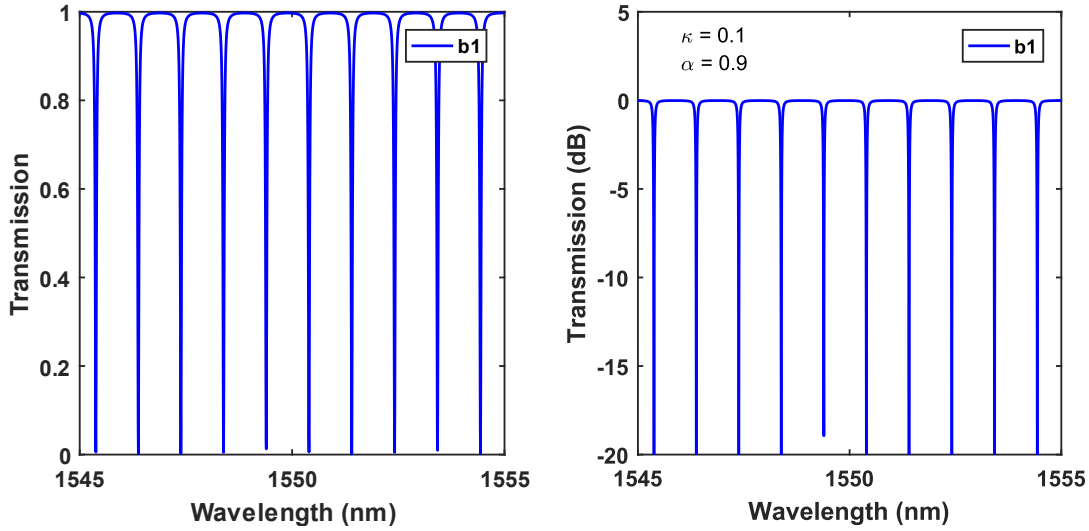

Figure 3.2: Intensity transmission response of a single ring coupled to a single bus waveguide in (left) linear scale and (right) logarithmic scale, with $\boldsymbol{R = 100\ \mu m}$, $\boldsymbol{n_g = 3.8}$, $\boldsymbol{\kappa = 0.1}$ and $\boldsymbol{\alpha = 0.9}$.

The ring resonator experiences a resonance condition when the transmission $|b_1|^2$ is minimized, i.e., the numerator is zero:

$$\alpha^2 + |t|^2 - 2\alpha|t|\cos(\theta + \phi) = 0$$

(3-9)

$$\frac{\alpha^2 + |t|^2}{2\alpha|t|} = \cos(\theta + \phi)$$

(3-10)

Considering the maximum values for α and t (i.e., $\max(\alpha) = \max(t) = 1$), then the above relation is valid when $\cos(\theta + \phi) = 1$, which occurs when $\theta + \phi = 2\pi m$, where $m = 0,1,2,\ldots$ is an integer. Due to the phase difference between t and $-\kappa^*$, $\phi = \pi$, and thus the resonance condition occurs when $\theta = \pi m$. At resonance then, the output is:

$$|b_1|^2 = \frac{\alpha^2 + |t|^2 - 2\alpha|t|}{1 + \alpha^2|t|^2 - 2\alpha|t|}$$

$$= \frac{(\alpha - |t|)^2}{(1 - \alpha|t|)^2} \tag{3-11}$$

A few cases for coupling exist, namely (**i**) under-, (**ii**) critical-, and (**iii**) over-coupling. The ring is critically coupled when $\alpha = 1 - \kappa = t$, as shown in Figure 3.3. However, how does one differentiate under- from over-coupling? The answer lies in the phase relation of the transmission response.

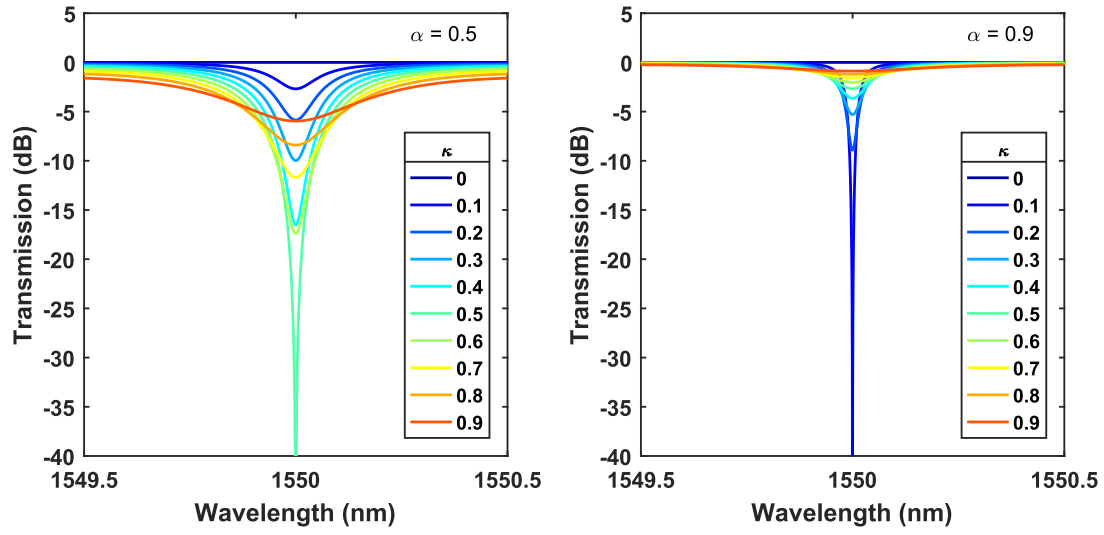

Figure 3.3: Intensity transmission response of a single ring coupled to a single bus waveguide with (left) $\boldsymbol{\alpha = 0.5}$ and (right) $\boldsymbol{\alpha = 0.9}$, with varying $\boldsymbol{\kappa}$. Critical coupling is achieved when $\boldsymbol{\alpha = 1 - \kappa = t}$.

In Figure 3.4, the transmission intensity and phase response are shown together. At the point of critical coupling, the phase varies between $\pm 90°$. As the coupling κ increases from 0 to ~1, the maximum change in phase $\Delta\Phi = \Delta(\theta + \phi)$ increases linearly up to a maximum phase change of $\pm 180°$ when $\kappa \sim 1$ [26]. In principle, it is very difficult to extract the state of coupling (i.e., under-, critical-, and over-) from the transmission response alone; the phase information is required to accurately determine the coupling state. One possible method for determining the phase response is to interferometrically combine the output of the ring resonator with a reference (uncoupled) waveguide. In this configuration, the phase response of the ring resonator is converted back into an amplitude response.

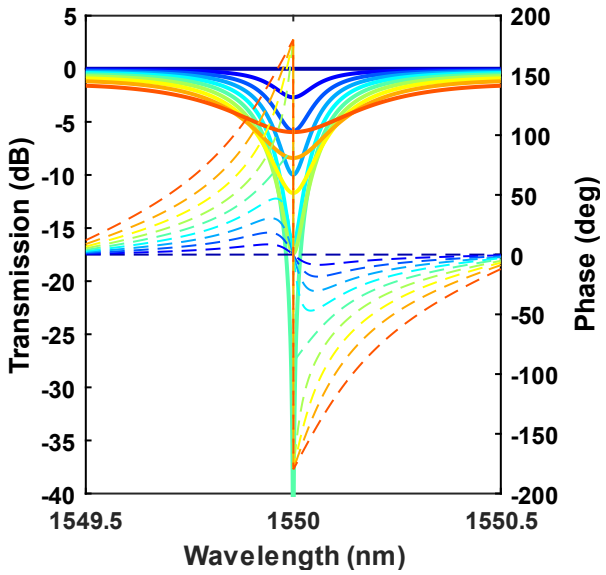

Figure 3.4: Intensity transmission (solid line) and phase (dashed line) response of a single ring coupled to a single bus waveguide with $\boldsymbol{\alpha = 0.5}$ and varying $\boldsymbol{\kappa}$.

3.2. Microring Resonators as Modulators

A microring resonator is configured as an electro-optic modulator by embedding a lateral p-n junction within the microring waveguide cavity [27] (see Figure 3.5). Through free-carrier plasma dispersion (FCD), injection or depletion of carriers changes the effective refractive index n_{eff} of the cavity, thereby changing the roundtrip phase θ, and altering the resonant wavelength λ_0 [28]. Placing a laser source with an emission wavelength close to λ_0, and applying a time-varying radio frequency signal across the p-n junction, will induce amplitude modulation of the laser emission wavelength corresponding to the RF input signal. The Si microring modulator device is based on a lateral Si p-n junction (~400 nm wide) on top of a buried oxide (BOX) layer, which also forms an optical waveguide (see Figure 3.6). The p- and n-contact regions are displaced away from the optical waveguide region (~1.6 µm), so as to not induce additional loss via free-carrier absorption (FCA).

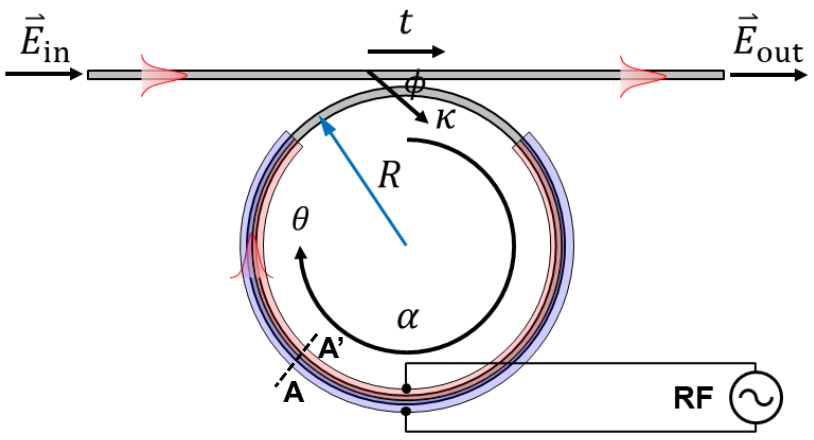

Figure 3.5: Schematic of an all-pass microring modulator, with an embedded p-n junction in the waveguide cavity, which primarily modulates the resonance by changing the round-trip phase when an RF signal is applied. Image from [22].

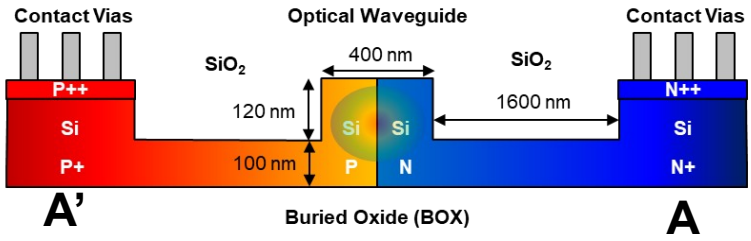

Figure 3.6: Cross-sectional view of a typical lateral p-n junction embedded in a ridge type waveguide, with top and bottom SiO_2 cladding. Image from [22].

The optical response of such a microring resonator was measured using an external cavity tunable laser, by sending the correctly polarized light (i.e., TE-pol) through the device and measuring the output into a photodetector. The separation between wavelength resonances is known as the free-spectral range (FSR), and from measurement was determined to be approximately 6 nm (see Figure 3.7). By applying a DC voltage to the p-n junction via Keithley 2401 source measurement unit, the resulting shift in resonance was measured.

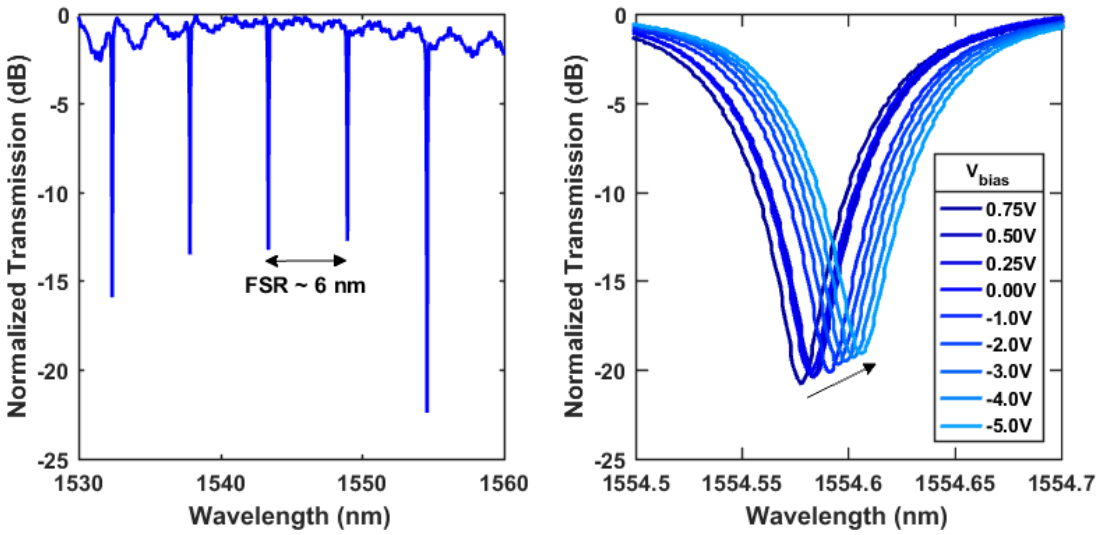

Figure 3.7: (Left) Normalized transmission DC spectral response of the Si ring resonator modulator from 1530 nm to 1560 nm, with a measured free-spectral range (FSR) of ~6 nm. Spectral response was taken at a DC bias voltage of 0.75 V. (Right) Normalized transmission DC spectral response of the Si ring resonator modulator as a function of DC bias voltage, V_{bias}, over a 0.2 nm span. The arrow indicates the shifting transmission function toward longer wavelengths and decreasing extinction ratio with decreasing bias voltage. Image from [21].

The RF electrical-to-optical (E/O) bandwidth of the Si RRM is determined by both the electrical RC parasitic time-constant τ_{RC} and cavity photon lifetime constant τ_p. For such small devices, the RC parasitics are very small, and the photon lifetime typically dominates the bandwidth. The photon lifetime is also directly proportional to the cavity quality factor, $Q = \lambda_m/\Delta\lambda = c/2\pi\tau_p\lambda_m$, which determines the maximum achievable extinction ratio (ER), or contrast between the digital '1' and '0' states. Thus, a trade-off in modulator performance exists between the Si RRM extinction ratio (ER) and RF bandwidth, assuming the device is photon-lifetime limited, which is illustrated by the simulation in Figure 3.8. A high Q or ER would allow for small modulation voltages, which is preferred to maintain compatibility with integrated circuits employing low voltage differential signals (LVDS).

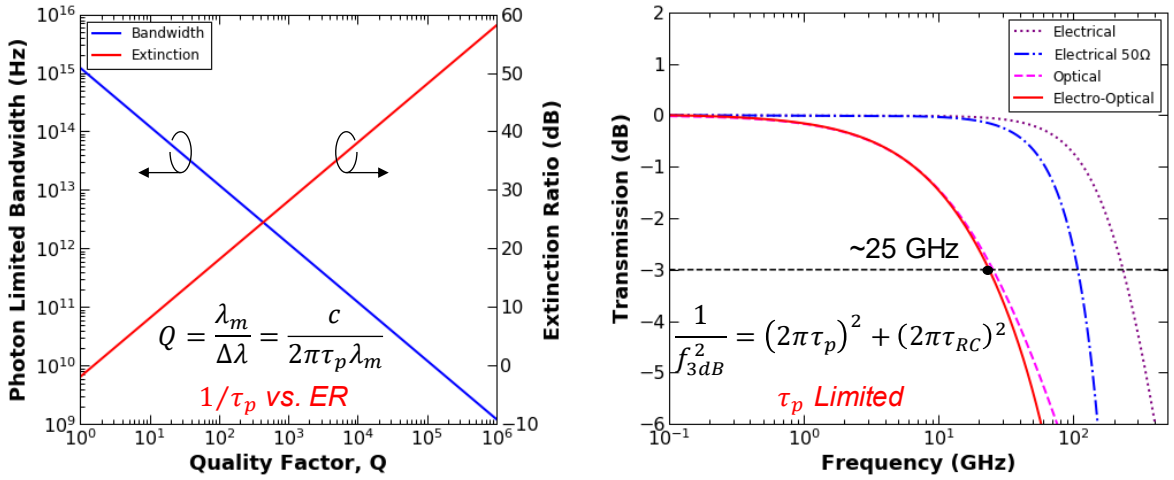

Figure 3.8: (Left) Modeled photon lifetime limited electrical-to-optical bandwidth and extinction ratio as a function of ring resonator modulator quality factor, Q. (Right) Modeled small-signal frequency transmission utilizing measured RC parasitics and photon-lifetime. Image from [22].

In Figure 3.9 the series resistance of the modulator was determined by measuring the current-voltage (I-V) response of the p-n junction and applying a linear fit to the curve under

forward bias. The capacitance of the modulator was determined by performing a capacitance-voltage (C-V) measurement on the device and using the value at high reverse bias.

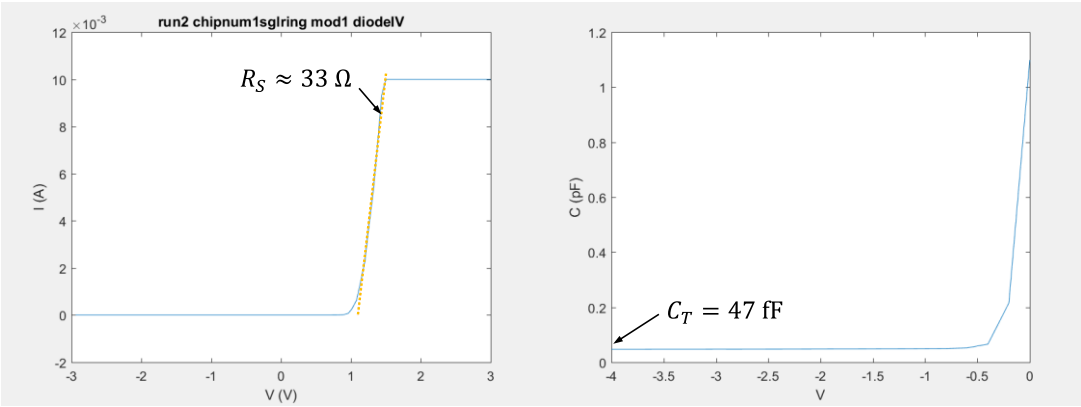

Figure 3.9: (Left) Measured current (A) as a function of applied voltage (V), from +3V to -3V, on the p-n junction, with a series resistance $R_S \approx 33\ \Omega$ from the linear fit. (Right) Measured capacitance (pF) as a function of applied voltage on the same p-n junction, with a total capacitance $C_T = 47$ fF at -4V.

By measuring the full-width at half-maximum of the Lorentzian lineshape resonance, the photon lifetime can be determined, and the -3dB point of the frequency response f_{3dB} of the modulator can be estimated using $f_{3dB}^{-2} = \left(2\pi\tau_p\right)^2 + (2\pi\tau_{RC})^2$. In Figure 3.8, the simulated frequency response is shown, in addition to the electrical- and optical-limited responses.

3.3.Small-Signal Modeling

A small-signal electrical equivalent model has been used to further describe the electro-optic response of the modulator, to describe the photon-lifetime limited characteristics of the modulator more accurately [29]. A Lorentzian lineshape was fit to a single resonance of the modulator, to extract both the ring-bus coupling lifetime τ_e and the roundtrip propagation lifetime τ_l, by considering the center resonance ω_r as:

$$T = \frac{P_{out}}{P_{in}} = \left| \frac{j(\omega - \omega_r) + 1/\tau_l - 1/\tau_e}{j(\omega - \omega_r) + 1/\tau_l + 1/\tau_e} \right|^2 .$$

(3-12)

As seen in Figure 3.10, the model fits reasonably well to the data, whereby the total photon lifetime is calculated as $\tau_{ph}^{-1} = \tau_e^{-1} + \tau_l^{-1}$. The model does takes into consideration both the optical fiber to chip coupling losses and waveguide to device loss; however, it does not account for potential on-chip reflections which result in the ripple that is noticeable in the baseline of the Lorenztian lineshape. The ripple does not appreciably impact the fit to model, as the deep resonance is the primary physical phenomena under consideration.

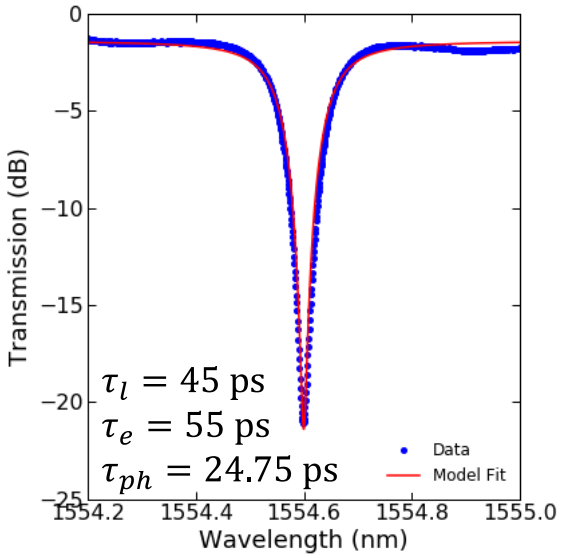

Figure 3.10: Lorentzian fit to a single resonance from a Si RRM device, to extract photon time-constants associated with waveguide bus-to-ring cavity coupling and ring propagation. Image from [22].

Using the previously measured values for the total series resistance $R_s = R_{cp} + R_{cn}$, where R_{cp} and R_{cn} are the p- and n-contact resistance, respectively, and total capacitance $C_{tot} = C_p + C_{si} + C_j$, where C_p is the pad capacitance, C_{si} or C_{ox} is the capacitance between the buried oxide (BOX) layer and the silicon substrate. The leakage current through the silicon

substrate is described by R_{si}, while the p-n junction resistance is R_j. A simplified equivalent-circuit model is given in Figure 3.11.

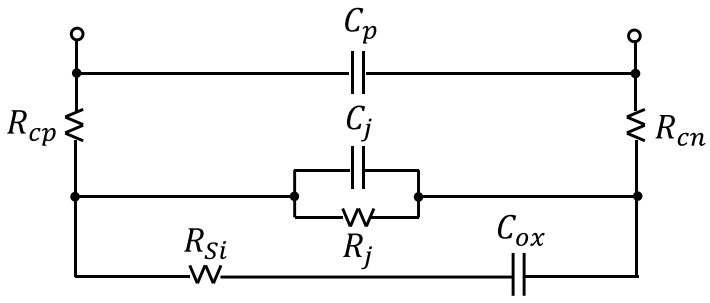

Figure 3.11: Small-signal equivalent circuit model for the microring modulator, incluing p- and n-pad coupling capacitance C_p, p- and n-contact resistance R_{cp} and R_{cn}, respectively, junction capacitance C_j, junction resistance R_j, silicon susbtrate leakage resistance R_{Si}, and buried oxide to silicon substrate capacitance C_{ox}. Image from [22].

Using a SPICE simulator, such as LTspice®, the total equivalent circuit model was constructed as shown in Figure 3.12. The circuit is comprised of two parts: (1) the electrical core and (2) the optical core. The electrical core is based on the previously measured values for total series resistance R_{tot} and total capacitance C_{tot}, and assuming reasonable values for each of the components comprising those values based on reported values in the literature.

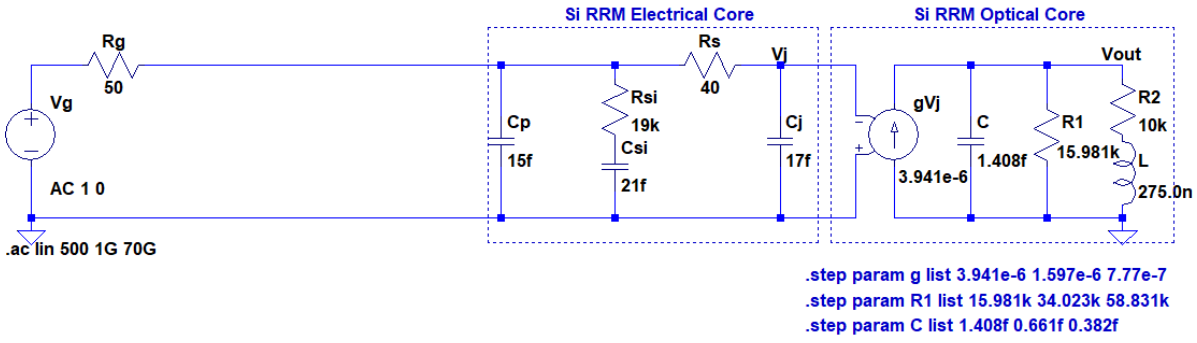

Figure 3.12: LTSpice schematic of the modeled Si RRM, including equivalent circuit parameters for the electrical and optical cores. Image from [22].

Using the following equations from [29] for the optical core equivalent circuit parameters, a complete circuit was modeled:

$$R_1 C = \frac{\tau_e}{2}$$

(3-13)

$$\frac{L}{R_2} = \frac{\tau_l}{2}$$

(3-14)

$$\frac{R_1}{R_2} = \frac{\tau_e \tau_l}{4}\left(\frac{1}{\tau_{ph}^2} + D^2\right) - 1$$

(3-15)

$$g = \frac{2}{n_{\text{eff0}}} \cdot \frac{\delta n_{\text{eff}}}{\delta V} \cdot \frac{\omega_r D}{R_1\left(D^2 + \tau_{ph}^{-2}\right)} \cdot U,$$

(3-16)

where D is a wavelength detuning factor, and U is a unit conversion factor so that the transconductance factor g has appropriate units. Using the SPICE simulation, frequency dependent transmission response of the modulator was modeled as a function of the wavelength detuning factor, in Figure 3.13. Depending on the amount of wavelength detuning, there is noticeable inductive peaking in the response, which can be attributed to the non-linear transfer function of the Lorentzian resonances lineshape below the FWHM point. The small-signal frequency response of the modulator was also characterized using a 67 GHz Agilent Lightwave Component Analyzer (LCA), whereby the laser was detuned by about 40 pm relative to the resonance. The model and measured small-signal frequency response show reasonable agreement in Figure 3.13.

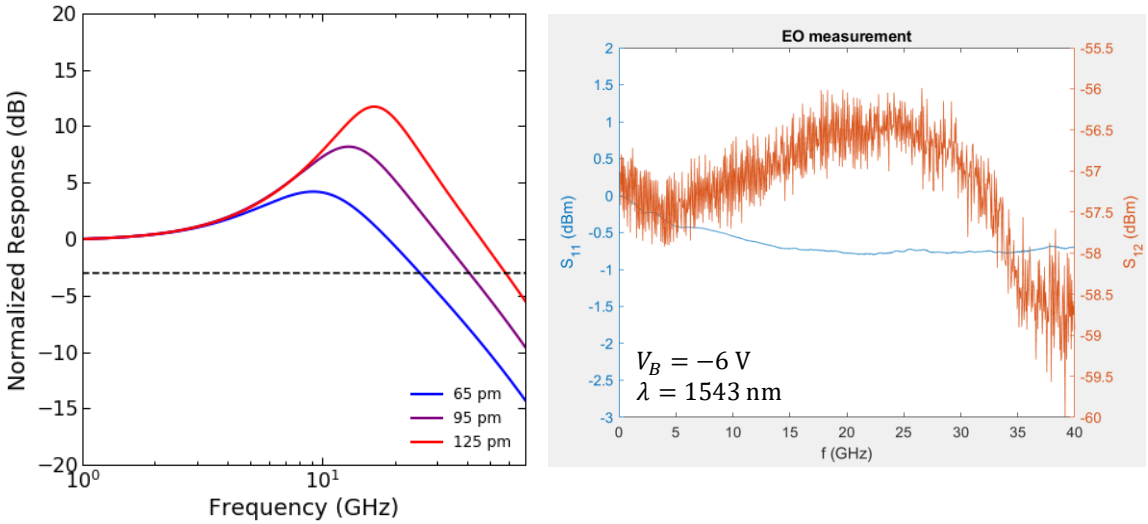

Figure 3.13: (Left) Modeled normalized response as a function of frequency for an Si RRM, with laser detunings of 65, 95, and 125 pm from resoances. (Right) Measured small-signal frequency response to 40 GHz. Image from [22].

3.4. Large-Signal Characterization

Next, the large-signal response of the microring modulator was characterized, using a high-speed pattern generator, according to the schematic of the test setup shown in Figure 3.14. A SHF 12105A bit pattern generator, with a pseudo-random bit sequence (PRBS) of 2^{31}-1 bit pattern length output signal, was configured to provide high-frequency content pre-emphasis. Using the two output channels from the pattern generator, with the same output signal, each signal was delayed by a fraction of the of the bit period using an ARRA variable delay line and combined with a 3-dB power splitter/combiner, and then amplified with a SHF 806E RF amplifier. The amplifier output was then sent through a bias-tee to provide a specific DC bias to the modulator device. To prevent a standing-wave between the modulator device and the amplifier output, a 3-dB attenuator was inserted between the bias-tee and the amplifier. The resulting signal was coupled into the modulator chip via a high-frequency probe, as shown in Figure 3.15.

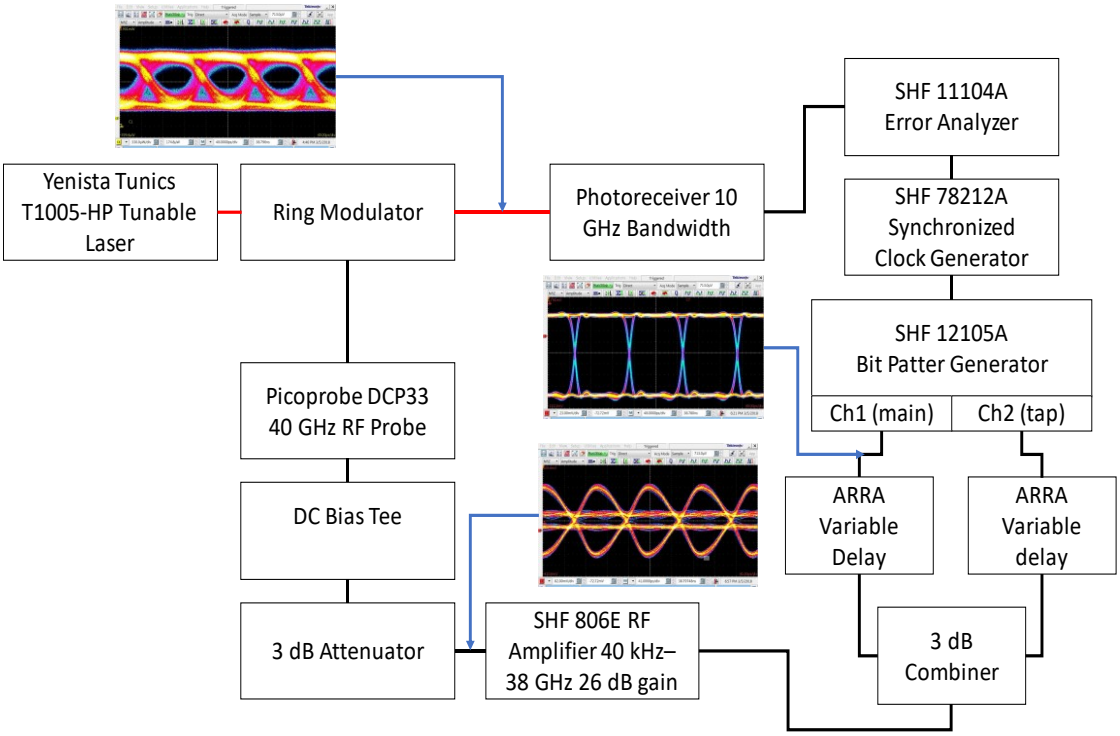

Figure 3.14: Schematic of large-signal test setup. Image from [21].

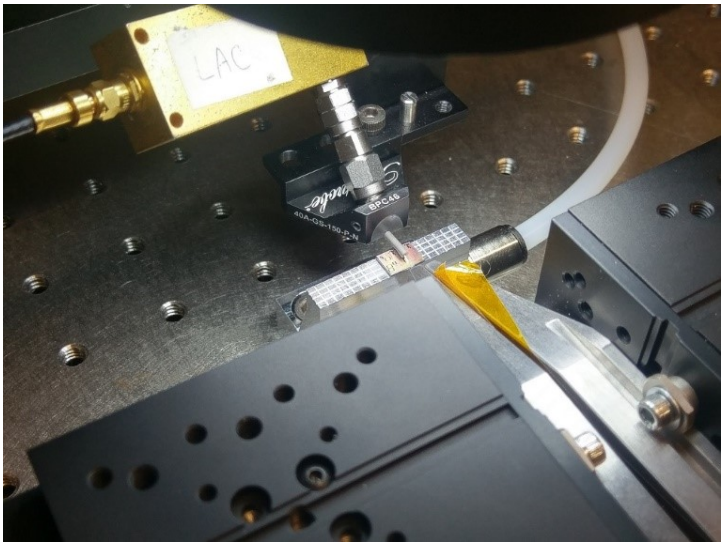

Figure 3.15: Photograph of Si RRM chip being tested on laboratory optical bench, with the signal coupled to the device through a bias-tee and RF probe, with optical fiber stages to couple light in and out of the chip. Image from [21].

Eye diagrams of the pre-emphasized input signals and resulting output signals from the microring modulator, at bitrates of 5, 8, and 10 Gbps, are shown in Figure 3.16. The emphasized high frequency content is noticeable as a large peak pulse within the PRBS bit stream, and the output eye diagrams are clear and open. A bit error rate (BER) measurement was made (see Figure 3.17), whereby a variable optical attenuator (VOA) was placed in-line between the output of the modulator and the input of the optical receiver, and the BER was measured as a function of the average received power (P_{avg}) and bitrate. The modulator was able to achieve BER < 1E-12 at 10 Gbps, which for many applications is considered "error-free". As expected, there is a power penalty between the bitrates of 5, 8, and 10 Gbps.

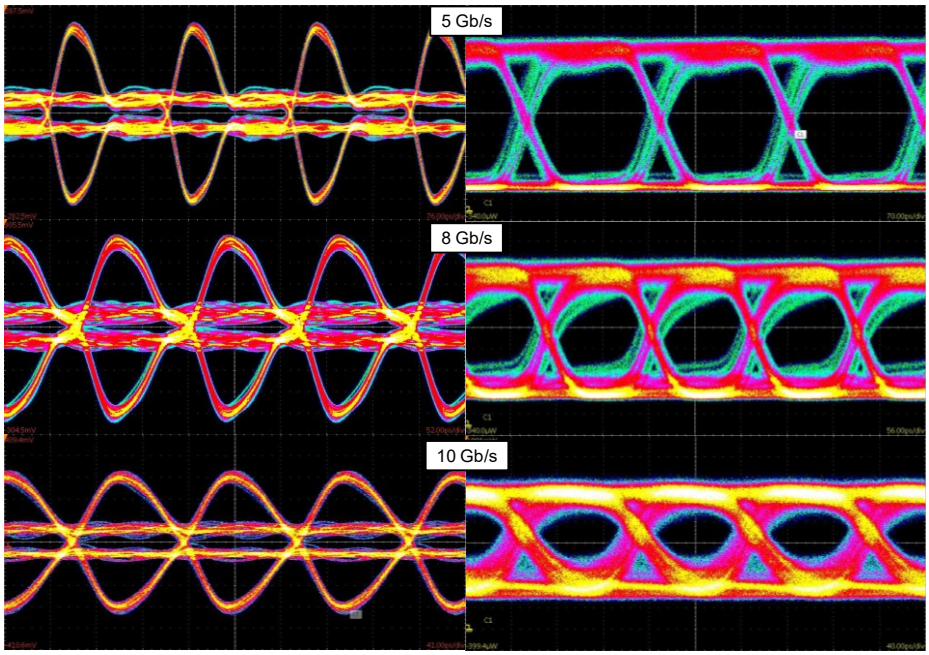

Figure 3.16: (Left) Input electrical eye-diagram waveforms after pre-emphasis, and (right) resulting output electrical waveforms from the Si RRM as a function of data rate, for 5, 8 and 10 Gbps from top to bottom. Image from [21].

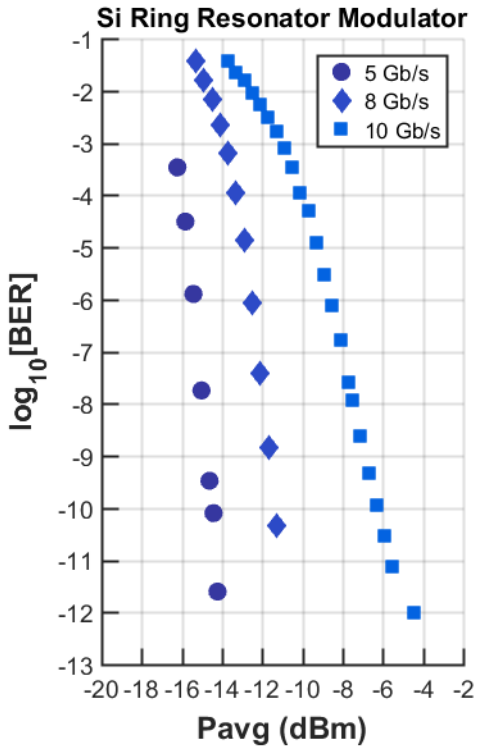

Figure 3.17: BER vs. receieved optical power at 5, 8 and 10 Gbps at ~1550 nm for the Si RRM, using 2^{31}-1 PRBS NRZ-OOK and achieving BER < 1E-12 at 10 Gbps. Image from [21].

Chapter 4 – CRYOGENIC OPTICAL LINK ARCHITECTURE

This chapter is based in part on the work in [1], [21], [22], and [30].

4.1. Motivation for Harsh Environment Optical Interconnects

Many applications benefit from operation at cryogenic temperature, despite the cooling energy overhead, including radio frequency (RF) and infrared (IR) sensing, semiconductor- and superconductor-based computing, etc. [31]. As the bandwidth requirements for these applications is ever increasing, new methods of high aggregate signal ingress and egress are needed that do not significantly contribute to thermal loading. Currently, metallic-based coaxial cables are used for signal ingress and egress from a cryogenic system, which have limited bandwidth (<20 GHz), high insertion loss (>3 dB/m), and high thermal conductivity (>10 W/m·K). Optical fiber on the other hand has very wide bandwidth (>6 THz), low insertion loss (<1 dB/km), and ultra-low thermal conductivity (<1 W/m·K), making it a preferable transmission medium of signals to/from ambient from/to cryogenic temperature environments. The challenge to date has been in realizing optical devices that operate efficiently at cryogenic temperatures, where the effects of carrier freeze-out can limit semiconductor-based devices [32], and the complexities/cost of hybrid integration limit the use of heterogenous materials, such as barium titanate ($BaTiO_3$) [33], graphene [34], and lithium niobate ($LiNbO_3$) [35]. Recent work has also shown the use of the DC Kerr effect in a silicon p-i-n modulator for operation well below carrier freeze-out [36], however reduced

RF drive voltages are needed to be compatible with CMOS electronics for high-speed digital applications.

In the case of a sensor sub-system, such as an IR focal plane array (FPA), the operating temperature is typically around liquid nitrogen (LN_2), i.e., ~77 K, where the effects of carrier freeze-out in most complimentary metal-oxide-semiconductor (CMOS) based readout integrated circuits (ROIC) can be designed around. Furthermore, next-generation ROICs are expected to support many 10s of Gbps aggregate data rates [37], although the maximum expected rates of individual electrical outputs are expected to be limited to ~2.5 Gbps in 90 nm / 180 nm nodes due to trade-offs in bit resolution, bandwidth, and output drive voltage. Digital ROICs (DROIC) are expected to leverage smaller process nodes (e.g., 65 nm) for larger format sensors, with ever-decreasing unit cell size, and vastly increased output data rates (e.g., 100 Gbps) [37]. Coupled with recent advances in monolithic photonic and electronic integration within commercial CMOS processes [38], the viability of producing cryogenic optical interconnects based on a silicon photonic platform are enticing for both classical and quantum applications. Silicon photonics offers multi-project wafer (MPW) fabrication for cost reduction, large aggregate signal bandwidth via techniques such as wavelength division multiplexing (WDM), and the ability for monolithic integration with electronics for sensing, communication, and computing systems at cryogenic temperatures. Here, the first demonstration of a novel link architecture for a cryogenic optical interconnect, with reduced thermal energy dissipation, is shown.

4.2. Components for Harsh Environment Optical Interconnects

The components for an optical interconnect deployed in a harsh environment will be discussed, ranging from the laser source to the optical receiver.

4.2.1. Light Sources

Optical interconnects are generally realized in two different manners with respect to the light source: (1) directly-modulated laser (DML), or (2) externally-modulated laser (EML). In DML type OIs, the choice of light source can be determined by the type of fiber and wavelength utilized: for single-mode fiber (SMF) based OIs, an edge-emitting type laser is used with an optical emission wavelength of 1.31 or 1.55 μm, whereas for multi-mode fiber (MMF) based OI's, a vertical- or edge-emitting laser is used with an on optical emission wavelength in the range of 0.85 to 1.55 μm. Typical edge-emitting DMLs include Fabry-Perot or distributed feedback (DFB) type lasers, with multi- or single-longitudinal mode profiles, respectively. For vertical-emitting DMLs, the vertical cavity surface emitting laser (VCSEL) is the primary laser type. The typical trade-off within DMLs is optical output power and modulation bandwidth. Edge-emitting lasers have longer optical cavities, allowing for higher photon density and thus higher average optical power, while vertical-emitting lasers tend to have lower output power, but can be modulated at higher-frequencies due to lower cavity lifetimes.

While DMLs offer reduced complexity of the OI architecture, further complications arise when they need to operate in the harsh environment. When subjected to cryogenic temperatures, the laser design must account for changes in optical gain medium and the cavity mirrors, leading to changes in optical emission wavelength. While this issue is less critical

when employed in an MMF based OI, this can present significant challenges if used with SMF in conjunction with other single-mode components, such as optical filters in a WDM configuration. Furthermore, DMLs are subject to optical frequency chirp, which can limit transmission distances, unless dispersion compensating fiber (DCF) is employed. When placed in a high-radiation environment, ionizing and non-ionizing radiation can lead to generation of traps from electron-hole pair (EHP) generation or vacancies, degrading device efficiency and output power with increasing dose.

Recent work has demonstrated the optimization of a directly-modulated VCSEL for cryogenic applications [39] and for high-energy physics (HEP) applications [40]. The IARPA *SuperCables* program sought to develop cryogenic OI to address emerging large-scale superconductor computing applications, however significant challenges remain. To address OI for high radiation environments, the Versatile Link (VL) and VL+ effort has utilized VCSELs and MMF for data egress from the ATLAS and CMS detectors at CERN.

4.2.2. Electro-Optic Modulators

It is preferable to implement an EML in the OI architecture, to reduce energy consumption and increase reliability. In fact, the two functions should be physically decoupled: the laser source should be placed in the benign environment while an external electro-optic modulator (EOM) is placed in the harsh environment to increase link design flexibility and reliability. While many materials have been investigated to modulate light, here the focus is on EOMs directly implemented in silicon photonic CMOS platforms that utilize P-N junctions. The P-N junction modulates both the intensity and phase of light when embedded in an optical

waveguide through the free-carrier plasma dispersion effect (PDE), described by the seminal Soref-Bennett equations [15].

Typically, silicon photonic EOMs are implemented in either a Mach-Zehnder interferometer or microring resonator configuration. In either implementation, it is the phase of the light that is manipulated, resulting in intensity modulation through coherent interference or resonance, in the case of a Mach-Zehnder modulator (MZM) or microring resonator modulator (MRM), respectively. The MZM has the advantages of relative insensitivity to optical wavelength and high electro-optic radiofrequency (RF) bandwidth, but with the potential disadvantages of high insertion loss and high switching voltage (i.e., V_π). The MRM on the other hand exhibits high sensitivity to optical wavelength and applied voltage – due to the resonant phenomena – in addition to high sensitivity to environmental perturbations (e.g., temperature or radiation).

When comparing MZMs to MRMs (see Figure 4.1), there is a notable advantage in the context of WDM OI, namely the "built-in" optical filtering of the MRM and significantly smaller footprint (e.g., ~50 μm^2 vs. ~10,000 μm^2 for MRM and MZM, respectively). For high WDM channel count applications (e.g., ≥4), it may be preferable to utilize MRMs to maximize both physical integration and aggregate bandwidth. Recent work has investigated the use of both MZMs [41] and MRMs [42] for harsh environment WDM OI, for high-energy physics (HEP) and cryogenic applications.

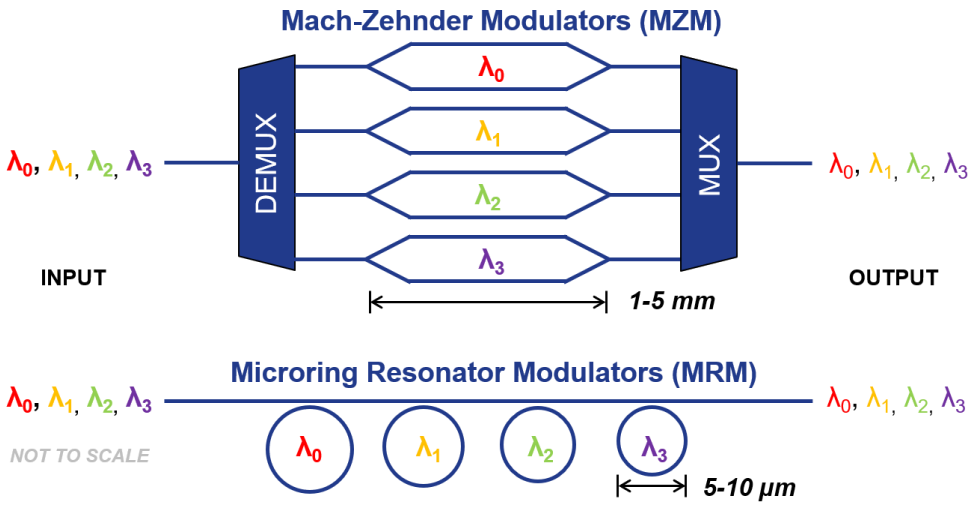

Figure 4.1: Comparison of an exemplary multi-channel WDM optical interconnect employing either an array of Mach-Zehnder Modulators (MZM) or an array of microring resonator modulators (MRM), whereby additional optical multiplexing (Mux) and demultiplexing (DeMux) components are needed on-chip. Image from [1].

4.2.3. Optical Receivers

Optical receivers (Rx) are typically implemented with either a simple P-I-N (PIN) photodiode or higher performing avalanche photodiode (APD) at the front-end, coupled to either a linear or limiting transimpedance amplifier (TIA) at the back-end. Depending on the OI link operating conditions and limitations, a PIN may be suitable where low-cost is critical and sufficient optical power is available, whereas an APD may be preferred for low optical power situations where higher cost can be tolerated. In addition, due to the avalanche process within the APD, the PIN may be preferred for higher opto-electronic RF bandwidth. Use of an optical Rx in a cryogenic environment almost always ensures operation in the shot-noise limit, as the thermal noise is negligible, for classical information. The low operating temperature does present challenges for APD Rx, as the breakdown or punch-through voltage point varies with temperature. For harsh environment OI, it is preferable to keep the optical Rx outside, as it is one of the most sensitive components in the link.

4.3. Optical Interconnect Design

The basic architecture design of the cryogenic optical interconnect is shown in Figure 4.2. The electrical outputs from a cryogenically cooled integrated circuit, housed within a cryostat or Dewar, drive electro-optic modulators (EOM) to optically encode the signal for information egress via optical fiber. Ring resonator modulators (RRM) coupled to a common bus waveguide are utilized as the EOMs, as they have a small footprint, require a low switching voltage, and can be modified to address individual WDM channels. While Mach-Zehnder modulator (MZM) based EOMs could be employed, additional heater elements are often needed to bias at quadrature, the associated high V_π requires larger drive voltages, and for WDM scaling, integrated wavelength filtering elements would be needed, adding loss and consuming a larger footprint. As shown in Figure 4.2, each RRM is addressed by an individual continuous-wave (CW) laser source and multiplexed (Mux) onto a single optical fiber. An example silicon photonic RRM, realized in the AIM Photonics multi-project wafer (MPW) process, is shown in Figure 4.3. An example link budget for a 1-, 4-, and 8-channel architecture is given in Appendix A.

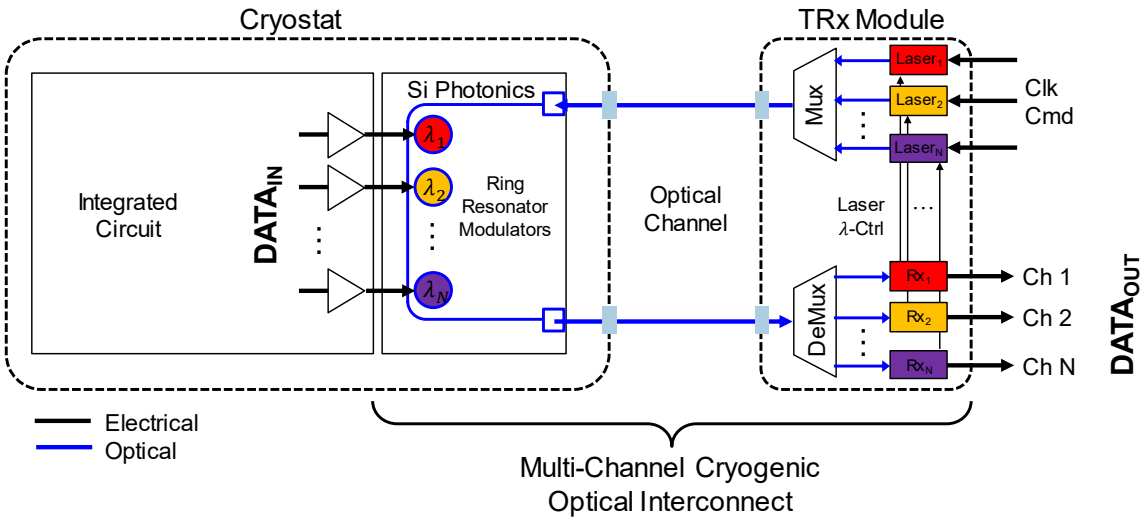

Figure 4.2: Architecture of a silicon photonic, multi-channel WDM-based cryogenic optical interconnect, utilizing remoted Si photonic ring resonator modulators (RRM) with input signals provided by a cryogenically cooled integrated circuit. Image from [30].

At the output of the RRMs, the optically encoded signals are demultiplexed (DeMux) and converted back into electrical domain signals via optical receivers (Rx). Due to their resonant operation, RRMs are sensitive to environmental perturbations, especially changes in temperature. For this reason, optical link implementations utilizing RRMs typically rely on integrated heaters to properly adjust the optical resonance relative to a fixed CW laser, via the thermo-optic effect [43]. Integrated heaters however can consume many 10s of milliwatts and dissipate unwanted heat into the cryogenic system, where cooling efficiency is quite low, and can add additional noise (i.e., Johnson) to the sub-system. Thermal noise is especially problematic in the context of scaling-up of quantum systems where the addition of thermal photons leads to qubit decoherence [44]. For these reasons, much development has been toward advanced integrated photonic technologies to interface with various quantum systems [45], to leverage increases in bandwidth, environmental isolation, lack of photon decoherence, and reduced size, weight, and consumed power (SWaP).

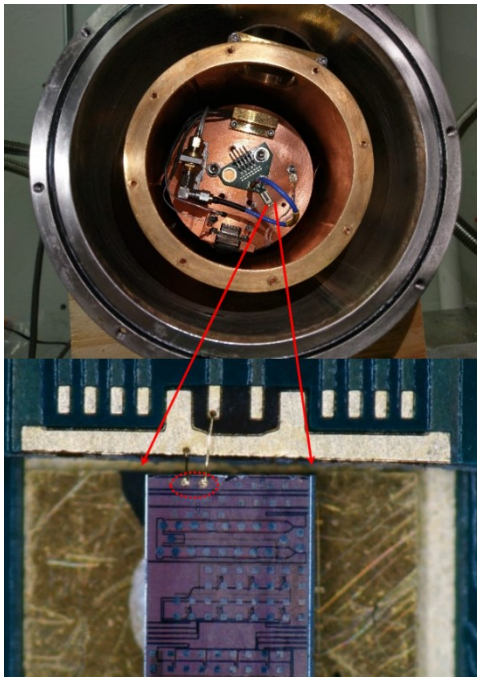

Figure 4.3: (Top) Photograph of 4K cryostat at Freedom Photonics with heat-shield and vacuum port removed, and the Si RRM mounted on a PCB on the Cu cold head in the center. (Bottom) Microscope image of the Si RRM mounted on the PCB, with arrows indicating chip location and dashed circle the wirebonded Si RRM device. Image from [21].

In the proposed architecture, local control of RRM resonance via integrated heaters is removed [43]. Instead, remote control is implemented by adjusting the CW laser emission from a tunable wavelength laser (see Figure 4.9). Monitoring the optical modulation amplitude (OMA) at the Rx allows the corresponding laser emission wavelength to be tuned using a feedback signal (λ-Ctrl), by locking to the appropriate operating point on the RRM transfer function. Now that the RRMs essentially operate in an "unlocked" manner, the Mux and DeMux components must be designed with passbands that accommodate the changes in resonance for each RRM-modulated WDM channel. The number of RRMs implemented, and their associated free-spectral range (FSR), set the Mux and DeMux passband, in addition to an upper-limit on the tolerable shift in RRM resonance for minimizing crosstalk between adjacent channels [46].

4.4.Silicon Photonic Ring Resonator Modulator

The custom designed silicon photonic RRM is shown in Figure 4.3 and was produced in AIM Photonics MPW fabrication run. Recent work has demonstrated cryogenic operation of RRMs also produced in AIM Photonics [47], further motivating this implementation. The chip was mounted on a custom printed circuit board (PCB) via electrically conductive epoxy, and wirebonded to a high-speed connector. At the benchtop-level, the voltage dependent spectral response was measured by sweeping an external cavity laser (ECL) across the optical C-band and measuring the optical power in a calibrated photodetector. For each sweep of the ECL, a DC bias voltage was applied to the p-n junction of the RRM, from -5V to 0V in 1V increments and from 0V to 0.75 in 0.25V increments. The voltage induced resonance shift is shown in Figure 4.4 and was measured to be 3.8 pm/V in the reverse bias regime.

In Figure 4.4, the anticipated OMA and extinction ratio (ER) were modeled using the measured voltage-dependent transmission data assuming DC bias of $V_{DC} = -3V$ and an RF voltage of $V_{RF} = 2V_{p-p}$. The ER was modeled by taking the difference between the transmission response at $V_{bias} = -2V$ and $V_{bias} = -4V$. The OMA was calculated by using the relationship between the ER and average optical power P_{avg}:

$$OMA = 2P_{avg}\frac{ER - 1}{ER + 1} \tag{4-1}$$

From the modeled data in Figure 4.4, the wavelengths resulting in maximum ER are not the same that result in maximum OMA. Since the OMA considers not only the RF modulation depth but also the average power (including optical loss), the principle of remote laser wavelength control of the RRM is to keep the laser emission wavelength at the point of

maximum OMA, despite changes in the RRM resonant wavelength induced by environmental changes.

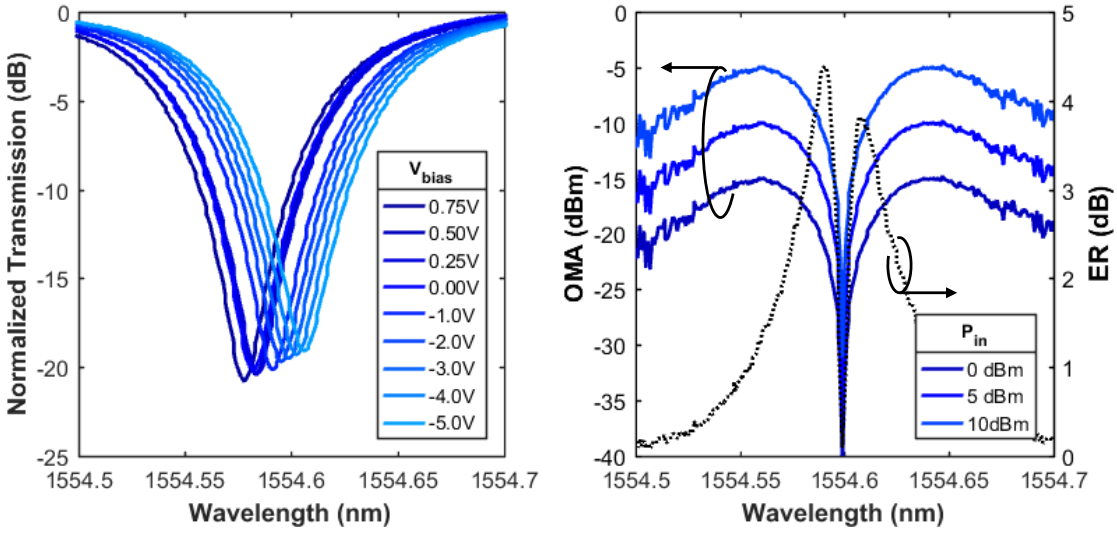

Figure 4.4: (Left) Measured normalized transmission of the modulator as a function of wavelength and DC bias voltage, from 0.75 V to -5.0V. (Right) Modeled optical modulation amplitude (OMA) and extinction ratio (ER) as a function of both optical wavelength and input optical power, P_{in}, assuming $V_{RF} = 2\ V_{p-p}$ and $V_{DC} = -3\ V$. Images from [22].

Changes in the environment's temperature have a significant effect on the resonant wavelength of an RRM. In Figure 4.5, the temperature dependent shift in RRM resonant wavelength is modeled for a 20 K change in temperature centered around two temperature ranges: 80 K (see Figure 4.5 (Left)) and 300 K (see Figure 4.5 (Right)), based on Eq. (3-8). For the same temperature change, the RRM experiences a smaller shift in resonance when operating at 80 K compared to operating at 300 K, due to the temperature dependent refractive index of the waveguide materials, known as the thermo-optic (TO) effect. Most of the power in the fundamental mode of the waveguide is constrained to the silicon, whereby the temperature dependent TO coefficient of silicon is much higher at 300 K compared to 80 K (~1E-4 T^{-1} vs. ~1E-5 T^{-1}, respectively) [48]. In Figure 4.6, the modeled behavior was confirmed by tracking the temperature induced changes in the RRM resonances as a function

of temperature. A tunable laser was swept across the resonances of the RRM at specific temperature intervals, from 300 K down to ~40 K, and the detected optical power was measured.

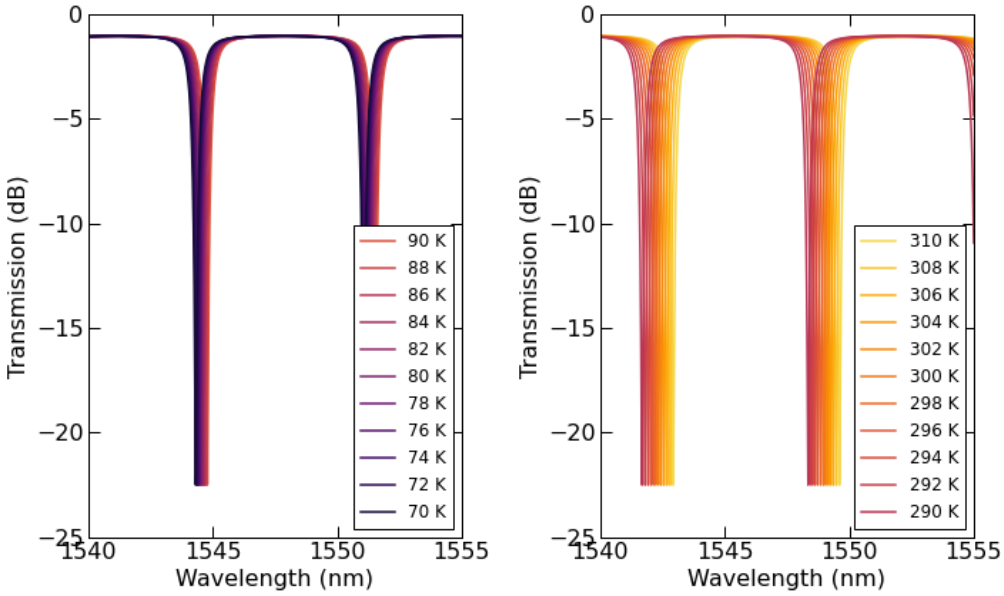

Figure 4.5: Modeled Si RRM transmission as a function of temperature for change of 20 K centered at (left) 80 K and (right) 300 K. Images from [22].

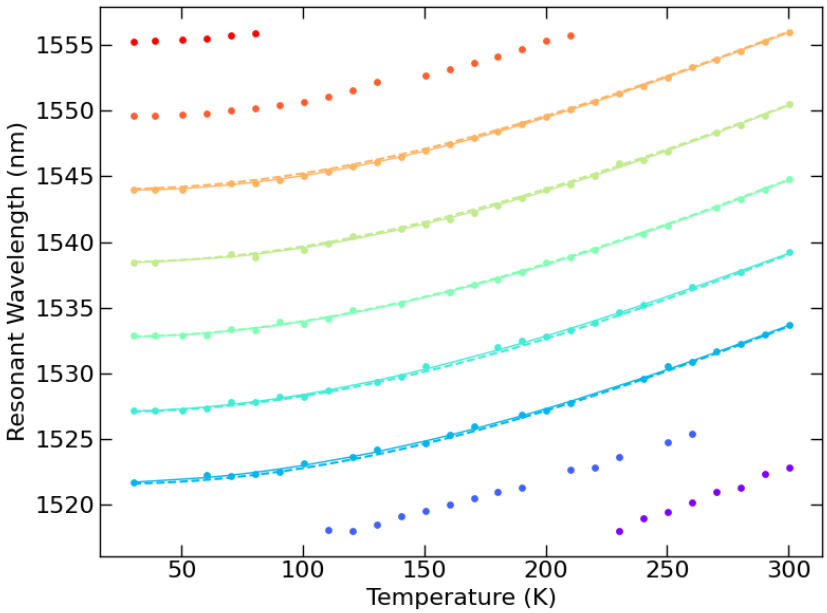

Figure 4.6: Measured shifts of multiple resonances of a Si RRM as a function of temperature, from 300 K to 40 K. Image from [22].

4.5. Cryogenic Optical Interconnect Experiment

The silicon photonic RRM is shown in Figure 4.3 and was produced in AIM Photonics MPW fabrication run. Recent work has demonstrated cryogenic operation of RRMs also produced in AIM Photonics [46], further motivating this implementation. In this experiment, the chip was mounted on a custom printed circuit board (PCB) via electrically conductive epoxy, and wirebonded to a high-speed connector. Tapered lensed-optical fiber assemblies (not shown) were the actively aligned to the edge-coupled waveguides of the RRM chip and mounted using an ultra-violet (UV) light cured epoxy.

A single-channel optical interconnect was then configured according to the schematic shown in Figure 4.7. The CW laser source was a Freedom Photonics FP4209 InstaTune^{TM}, tunable over a 40 nm range centered at 1550 nm, and capable of arbitrarily switching between 10,000 calibrated points in under 2 μs. The laser output was first sent through an optional 26-dB gain erbium-doped fiber amplifier (EDFA), then through fiber polarization rotator (Pol.Rot.) paddles, before entering (and exiting) the cryostat via fiber-optic vacuum feedthroughs. The modulated output signal was sent through a second EDFA, a tunable bandpass filter (T-BPF) to suppress amplified spontaneous emission (ASE) noise, and a variable optical attenuator (VOA) before photodetection in a 10 Gbps optical receiver (Rx). The input electrical signal was a 2^7–1 pseudo-random bit sequence (PRBS), supplied by a pulse-pattern generator (PPG) operating at 2.5 Gbps. ROICs typically employ 8b/10b encoding, which can be approximated by a 2^7–1 PRBS. To compensate for the coaxial cable losses, a 17-dB radio frequency (RF) amplifier was placed in-line between the PPG and the RRM. Finally, the optical Rx output was sent into a digital communications analyzer (DCA) for eye diagram capture or an error detector (ED) for bit error rate (BER) measurements.

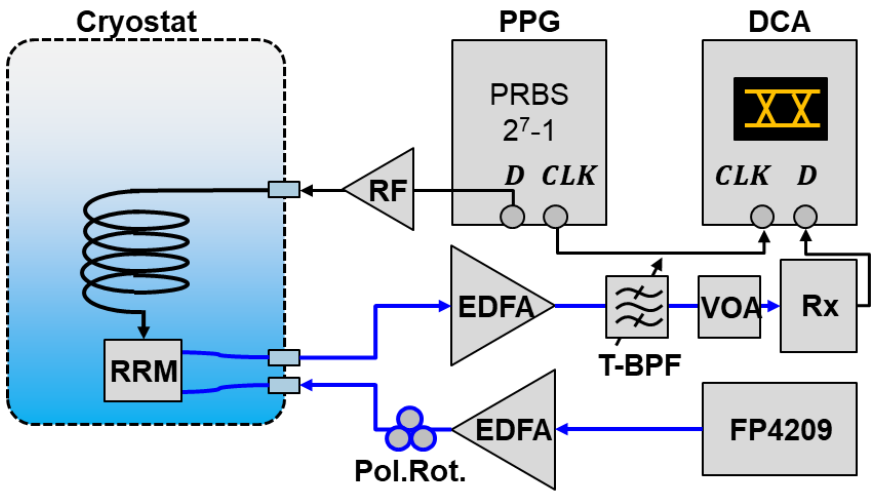

Figure 4.7: Block diagram of cryogenic optical link experimental setup. Erbium doped fiber amplifier (EDFA), polarization rotator (Pol. Rot.), ring resonator modulator (RRM), tunable optical bandpass filter (T-BPF), variable optical attenuator (VOA), optical receiver (Rx), digital component analyzer (DCA), pulse pattern generator (PPG), RF amplifier (RF). Image from [30].

The BER was measured as a function of received average power at the Rx, with the RRM operating at 300 K and 80 K. As shown in Figure 4.8, the RRM achieved BER <1E-10 at 300 K and BER <1E-5 at 80 K, both at 2.5 Gbps. As discussed above, the 2.5 Gbps channel rate is governed by ROIC subsystem design optimization. The RRMs themselves can achieve much faster modulation, with prior results demonstrating 40 GHz bandwidth and 20 Gbps operation at 300 K [22]. Corresponding eye diagrams are shown in Figure 4.8, with increased jitter at 80 K. As a result of the thermally induced changes in fiber coupling efficiency, a 10-dB power penalty was observed between 300 K and 80 K. The coupling loss can be further improved through optimized coefficient of thermal expansion (CTE) matching, whereby the temperature dependent CTE of the materials involved must be accounted for.

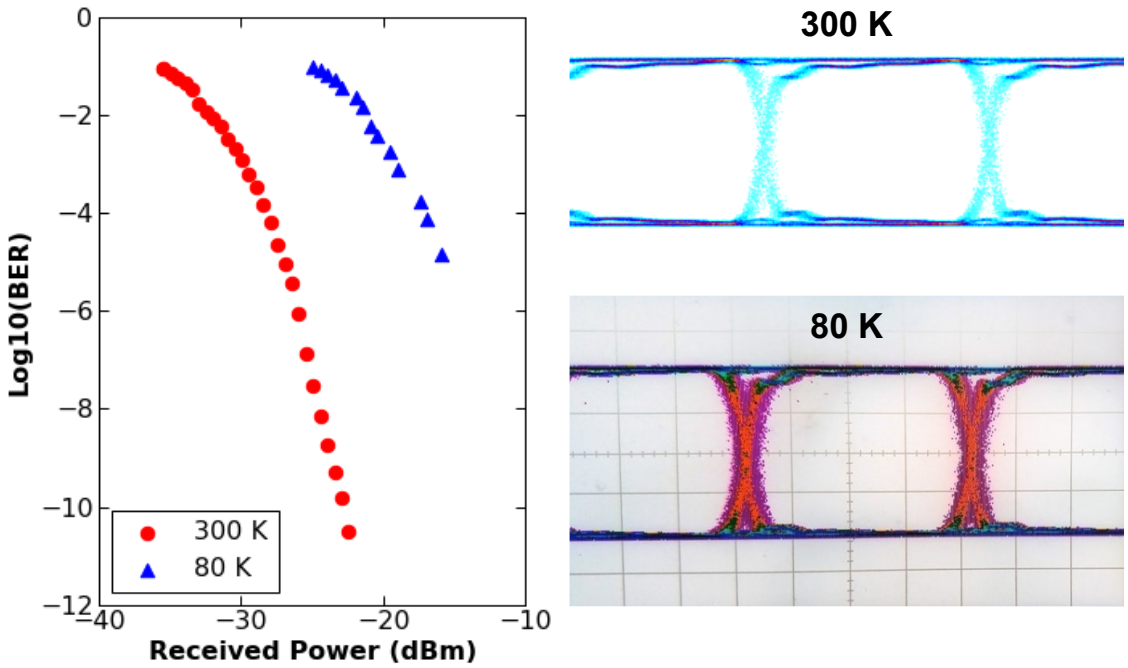

Figure 4.8: (a) Measured optical link bit error rate as a function of time-averaged received power at the optical receiver, when the RRM is at a temperature of 300 K and 80 K, with corresponding eye diagrams in (b) and (c), respectively. Data measured at a bitrate of 2.5 Gbps, $V_{RF} = 2\ V_{p-p}$, and $V_{DC} = -3\ V$. Image from [30].

4.6. Remote Laser Wavelength Control

Control of microring modulator is typically achieved by using an integrated heater, in the form of a resistor, to locally heat the device and adjust the resoance through the thermo-optic effect [43]. In a cryogenic application, this approach is not favorable due to extra heat dissipation and increased cooling power [31]. Prior methods to control a reasonant cavity include the Pound-Drever-Hall method [49], dithering signals [50], monitoring of link BER on-chip [51], monitoring defect induced photocurrent [52], balanced homodyne detection [53], and coherent detection with laser feedback control [54]. In this implementation, control of the modulator is achieved by monitoring the RF power within a narrow frequeny range at the optical receiver, and using the proportional output voltage as an error signal to be digitized and used in a digital control of the tunable laser wavelength emission. As shown in the block

diagram of Figure 4.9, the RRM is modulated by an input signal ($DATA_{in}$), and the RF power detector circuitry is designed to monitor the received signal at the optical reciever ($DATA_{out}$), whereby the OMA is directly proportional to the RF power. The tunable laser module contains a micrcontroller with internal memory and system clock, such that the RF power signal is periodically sampled and compared against the previously measured value. If the signal is within a tolerable range (e.g., ±5%), the laser wavelength is not adjusted. If however the signal falls outside that range, then the laser enters a narrow search mode, whereby (i) the wavelength is increased and decreased by an equal amount away from the last value, (ii) the corresponding RF power is determined, and the wavelength is readjusted in the direction of increasing power, (iii) until a maximum value is achieved again. Some amount of calibration is required beforehand, as the Q-factor of the RRM determines the sensitivity of the loop, and the corresponding loop amplifier gain needs to be adjusted.

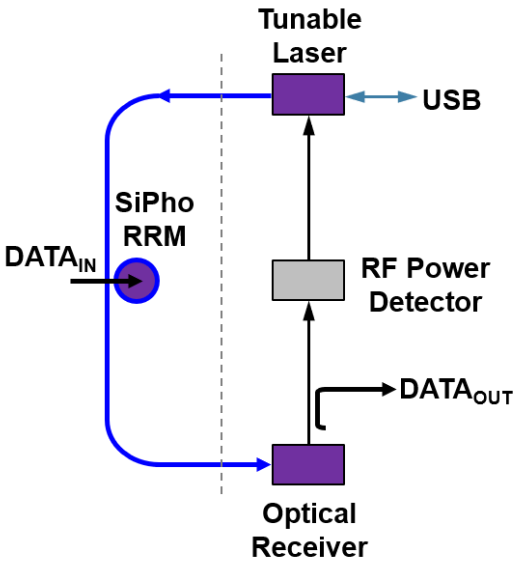

Figure 4.9: Block diagram for a single WDM channel laser wavelength locking loop, whereby a fraction of the output data signal is sent into an RF power detector and sends a voltage signal back into the tunable laser module for analog-to-digital conversion and decision logic making. Image from [30].

To demonstrate the principle of "remote" control of the RRM resonance via laser wavelength tuning, FP4209 laser was linearly swept across the C-band while the RRM was modulated at 2.5 Gbps at 300 K. Part of the Rx output signal went into an RF power meter, with a voltage output proportional to the RF power in the signal and is equivalent to the OMA. The measured wavelength-dependent RF power is shown in Figure 4.10(Left), whereby a single RRM resonance is shown, with two peaks in the RF power due to operation on either side of the Lorentzian line shape of the RRM resonance. Eye diagrams were captured at various indicated operating points, with the best result obtained at the peak RF power point (see Figure 4.10 (Right)). As the laser is tuned away from the peak RF power, the quality of the eye diagram degrades. The output signal from an RF power meter can be used to actively tune and lock the laser where optimized operation is achieved. Although this demonstration was performed at 300 K, the temperature dependent thermo-optic coefficient of silicon is much higher at 300 K compared to 80 K (~1E-4 T^{-1} vs. ~1E-5 T^{-1}, respectively) [48]; thus, locking of the laser wavelength to the RRM under dynamic thermal conditions at 80 K requires smaller laser wavelength adjustments than at 300 K due to lower thermal sensitivity of the RRM. Furthermore, since the lifetime of two-photon absorption generated free carriers is significantly smaller (e.g., 100 ps at 5 K) than the long thermo-optic relaxation lifetime (e.g., 133 ns at 5 K), allowing for electrical pulse sequences of 10s of ns to remain on-resonance and simplified thermal control of the RRM [55].

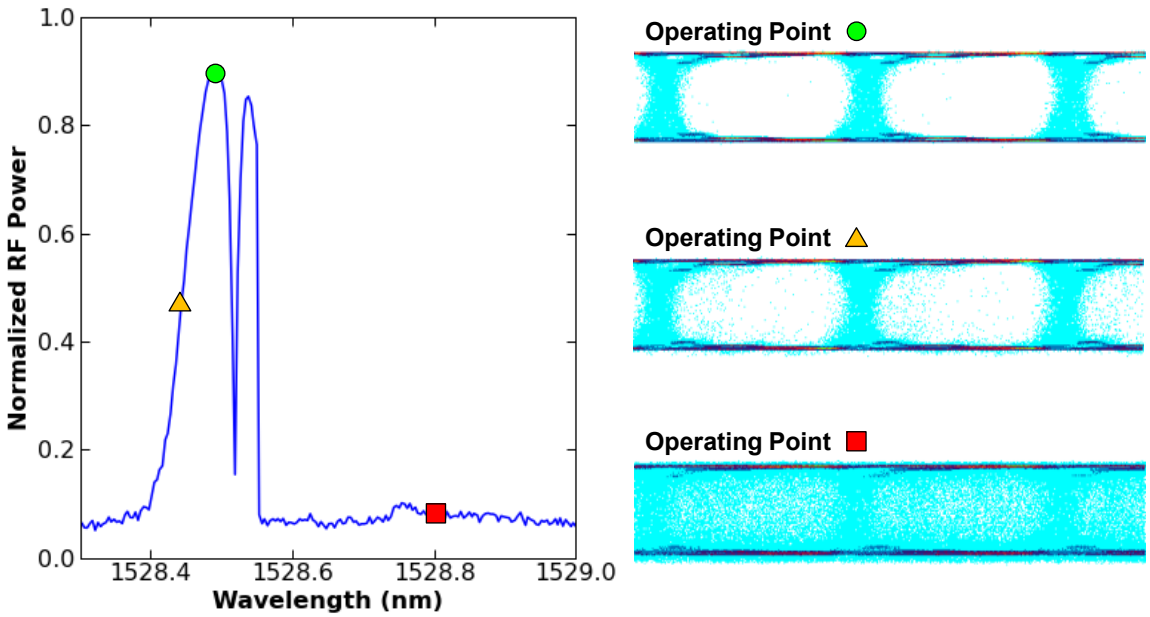

Figure 4.10: (Left) Measured RF power in the output modulation signal of the RRM as a function of optical wavelength, with a PRBS 27-1 input signal at 2.5 Gbps, $V_{RF} = 2\,V_{p-p}$, and $V_{DC} = -3\,V$. (Right) Eye diagrams captured at various RF power points, with the best performance achieved at the highest RF power. Image from [30].

To further demonstrate the wavelength locking operation, the Si RRM device was placed on temperature-controlled mount, modulated at 2.5 Gbps, and the temperature of the device was ramped from 50C to 25C in about 2.2 ms (see Figure 4.11(Top)). As the modulator was temperature tuned, the wavelength locking loop adjusted the emission wavelength the FP4209 laser (see Figure 4.11(Middle) to maintain maximum RF power (see Figure 4.11(Bottom). In the regions where the laser wavelength appears to have a small linear change with time, the locking circuit can maintain maximum RF power. Regions where the wavelength changes dramatically correspond to loss of locking, and the inverted RF power output signal (high). Further work is required to fine-tune the locking algorithm and allow for tracking over a broader wavelength range. For some applications at cryogenic temperatures (e.g., inside a dilution refrigerator), the environment may only change by a few Kelvin, which would make

this wavelength locking approach well suited. In other applications, the ambient temperature may change by many 10s C, and would require better locking operation.

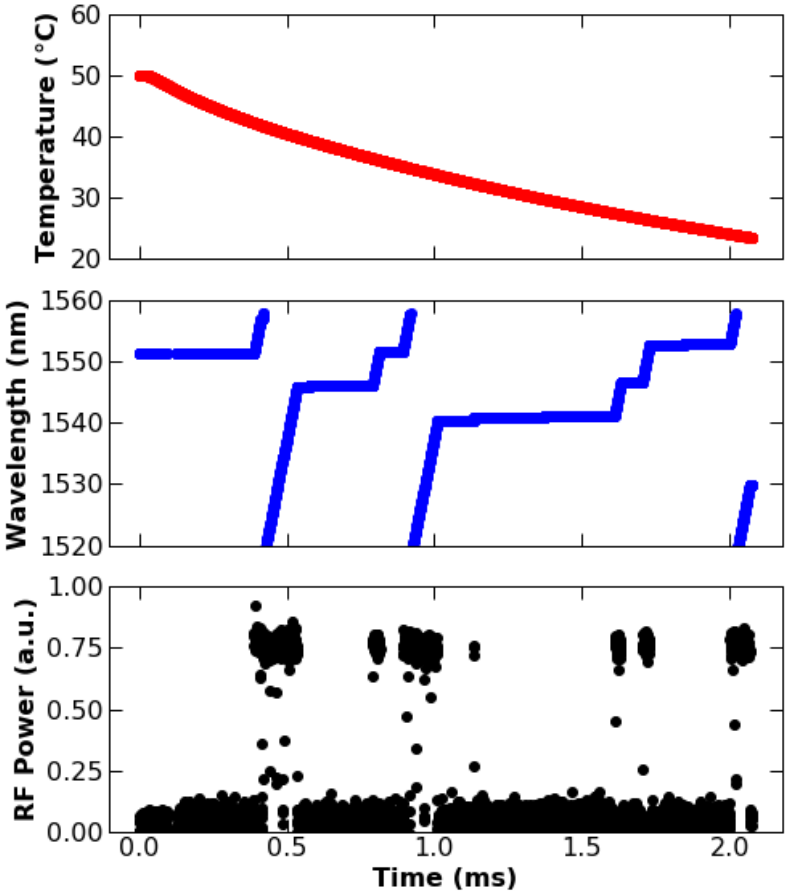

Figure 4.11: (Top) Temperature of the SiPho RRM as a function of time. (Middle) Emission wavelength from FP4209 tunable laser as a function of time, changing in one direction to achieve maximum RF power. (Bottom) Measured RF power as the laser emission wavelength changes. Low signal corresponds to high RF power while a high signal corresponds to low RF power.

Chapter 5 – RADIATION HARDENED OPTICAL LINK ARCHITECTURE

This chapter is based in part on the work in [1].

The design considerations for an optical interconnect deployed in a harsh environment will be discussed, ranging from the device physics up to link level design and optimization.

5.1. Device Simulation and Design

Silicon photonic based EOMs leverage the free-carrier PDE to modulate the phase of light as it travels through a P-N junction. This physical process also imparts a change in amplitude through the Kramers-Kronig dispersion relation [15].

In SiPho EOMs, ionizing radiation causes holes to build up in the bulk oxide, as well as in the Si-SiO_2 interface. This buildup then displaces holes within the p-doped Si region, leading to a pinch-off of hole density between the P region of the junction and the P contact, effectively disconnecting the two regions and resulting in device failure. Prior work has shown that radiation hardness in SiPho EOMs improves as the thickness of the Si slab below the P-N junction increases [55]. Additionally, increasing the density of holes in the p-doped Si slab improve the radiation hardness of the device, by increasing the number of holes required at the Si-SiO_2 interface to displace the p-implants. Utilizing both a shallow etch and high dopant concentrations is expected to improve the radiation hardness of SiPho modulators significantly.

First, a 90 nm silicon-on-insulator (SOI) commercial SiPho process was examined (see Figure 5.1), and a deep-etch Si EOM was modeled using various commercial software packages (see Figure 5.2). Radiation modeling was performed using the Synopsys Sentaurus TCAD software suite, with device geometry, meshing, and doping profiles set in Sentaurus Device Editor (SDE) and gamma radiation/trap generation being done in Sentaurus Device (SDevice) with the device held at a 1V reverse bias throughout the radiation simulation. Finally, the simulated devices were passed into RSoft BeamPROP to solve for effective index. These simulations were based on the work done by [55], with the addition of current-voltage characteristics added to the workflow.

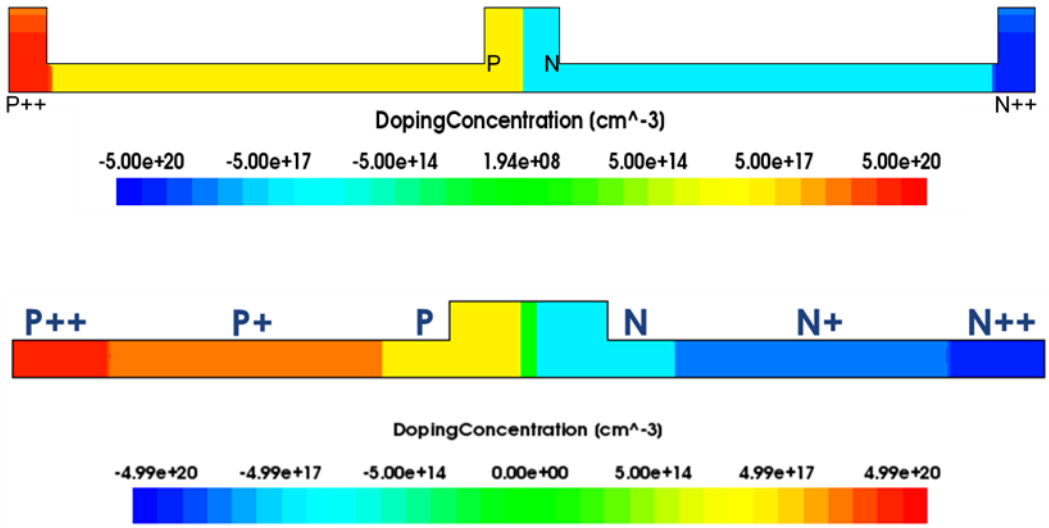

Figure 5.1: Doping profile for (Top) the 90 nm SOI photonic process and (Bottom) 180 nm SOI photonic process, used in the TCAD simulations. Image from [1].

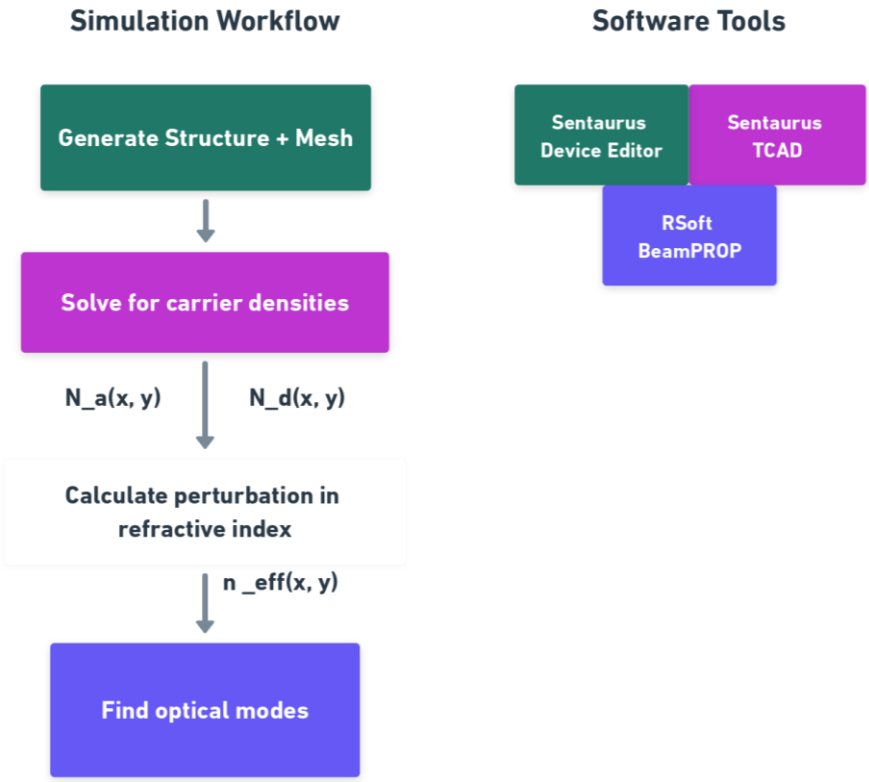

Figure 5.2: TID radiation simulation workflow using commercial software tools from Synopsis, whereby (i) the physical structure is generated and meshed using Sentarus Device Editor, (ii) the device is irradiated with a gamma ray model and the resulting carrier densities are calculated including appropriate trap models in Sentarus TCAD, (iii) the change in carrier densities are mapped to changes in the real and imaginary components of the refractive indices via the Soref-Bennett equations, and finally (iv) the resulting complex effective index of the propagating modes are calculated using RSoft BeamPROP. Image from [1].

In Figure 5.3(a), simulated ionizing radiation creates a discontinuity in the density of holes between the N-contact and the N-region of the phase shifter, due to the trapping of holes in the interface between the Si slab and the SiO_2. The device can tolerate higher total ionizing dose (TID) before failing (i.e., the TID at which the pinch off occurs) by either (i) increasing the concentration of carriers (i.e., using a higher dopant concentration) throughout the slab, (ii) increasing the thickness of the slab (i.e., decreasing the etch depth), or (iii) decreasing the gap between the N-contact and the N-region of the phase shifter.

Current-voltage characteristics were also modeled for the device (see Figure 5.3 (b)) between -2V and 1.5V. These correlate well with the aforementioned pinch off of the hole density in the EOM, as well as data from the literature [57], in that the depletion of holes between the N contact and N region of the phase shifter – caused by ionizing radiation – is the result of interface trap generation in the SiO_2 layers, thus creating a parallel path for current to travel around the device rather than through it. This results in both an increase in leakage current in the reverse bias and an increase in the series resistance of the device, evident in the forward bias. Finally, the effective index of this device was modeled at various doses of ionizing radiation, from which the phase efficiency was calculated (see Figure 5.3 (c)). The simulations suggest that both this maximum point will shift to slightly larger reverse bias (~ -0.2V), and the overall phase efficiency will be decreased significantly as a function of TID. This seems to suggest that the device is still somewhat able to modulate after the hole density pinches off before 500 krad and that if kept at a low bias, may be able to survive at a slightly larger TID than is predicted by the hole density pinch off.

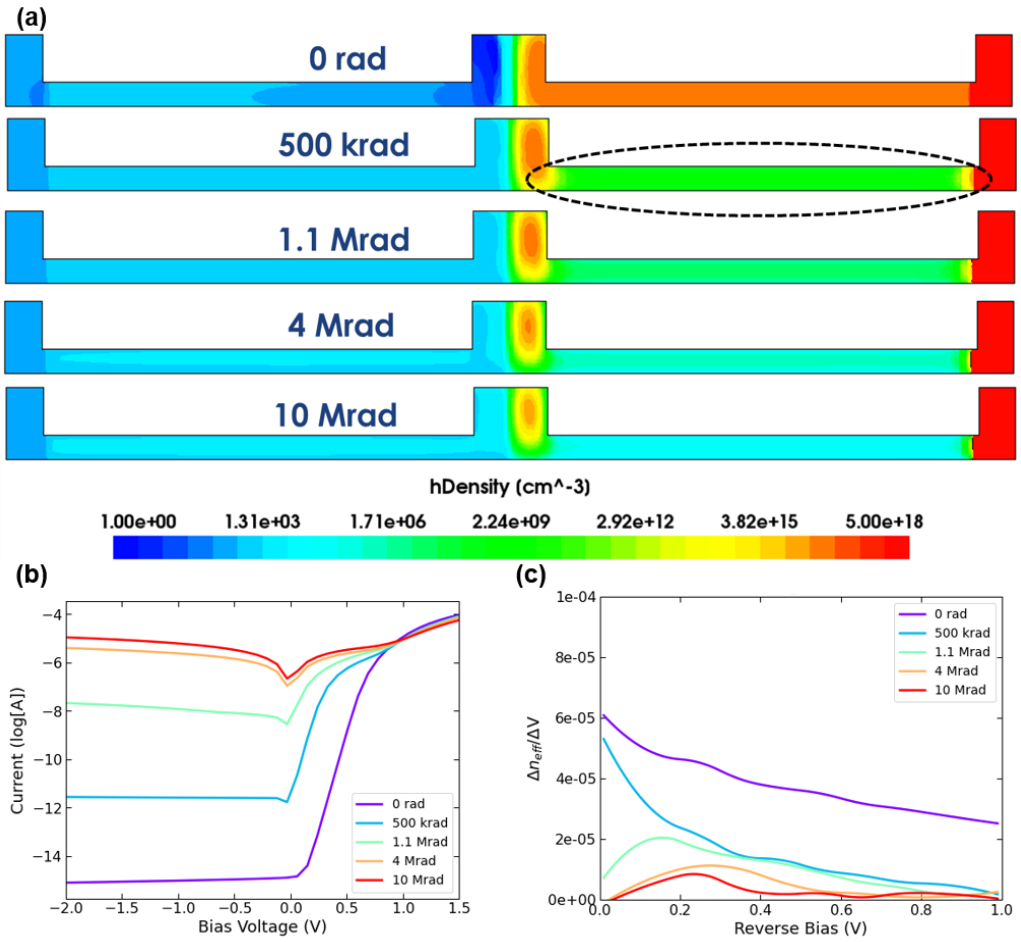

Figure 5.3: (a) Simulated hole carrier density in a 90 nm SOI lateral P-N junction embedded deeply etched slab waveguide, as a function of TID, with pinch off occurring in the P-doped slab region at ~500 krad. (b) Simulated current-voltage response of the corresponding P-N junction as a function of TID. (c) Simulated change in effective modal index (Δn_{eff}) with change in applied voltage (ΔV), as a function of TID utilizing the Soref-Bennett equations. Image from [1].

In addition to the lateral P-N junction phase shifter analyzed in Figure 5.3, a P-I-N junction phase shifter from a commercial 180 nm SOI SiPho process was also examined. The doping profiles for this device were unknown, so the same approximate profiles were used for the contact regions (here P^{++} and N^{++}) and for the P- and N- regions (see Figure 5.1). The additional P^{+} and N^{+} regions were doped with ~1E18 cm^{-3} of boron and phosphorous, respectively. One of the key differences between this geometry and that of the 90 nm SOI device is that the Si etch is much shallower – with the ridge at only twice the height of the

slab – compared to three times the height of the slab in the 90 nm SOI device. The same simulation workflow used for the 90 nm SOI process was used (see Figure 5.2). A cross-section of the 180 nm SOI lateral P-I-N junction, as a function of TID, is shown in Figure 5.4(a). In this device, the pinch off occurs after 10 Mrad, much later than in the 90 nm SOI device. In Figure 5.4(b) the current-voltage characteristics are shown, and do not appear to have a significant increase in leakage current, though that is expected after the pinch off occurs above 10 Mrad. The effective index trend of the 180 nm SOI device is similar to that of the 90 nm SOI device in that it demonstrates a drop-off in phase efficiency as the reverse bias gets larger, as well as having a steeper slope before this point as the TID is increased. However, the overall phase efficiency of this device is higher, likely due to the higher overlap between the mode and the slab and the charge carriers therein, thus, via the Soref-Bennett equations, a larger change in effective index for the mode.

The 180 nm SOI SiPho process is promising for increased radiation hardness, through a combination of (i) intrinsically supporting a thicker slab waveguide region, and (ii) utilizing highly doped (HD) P- and N-regions in the waveguiding region. This process warrants further study for achieving >100 Mrad TID operation for the most demanding applications, like OI for tracking detectors in HEP. The P-N junction modifications also need to be considered in terms of device bandwidth, as it has been shown in other work [58] that the reduced carrier densities from TID can lead to an RC parasitic limited bandwidth.

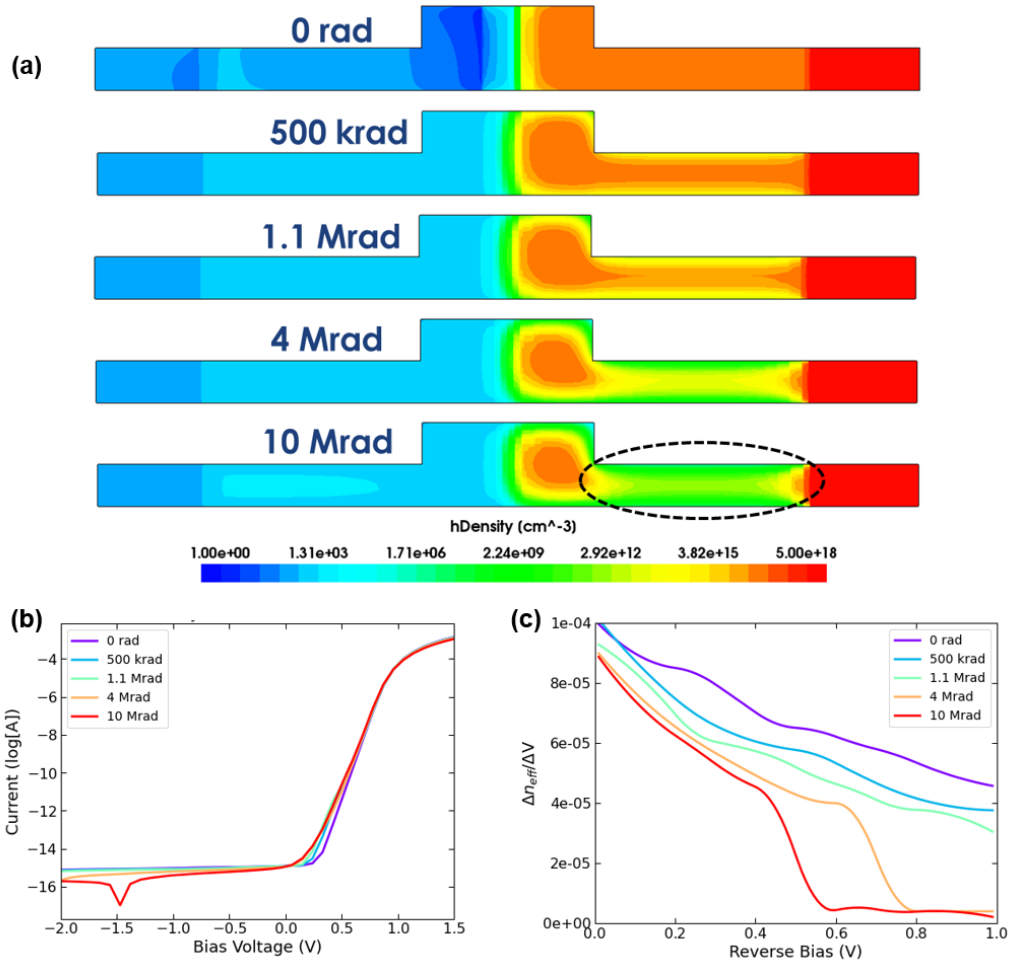

Figure 5.4. (a) Simulated hole carrier density in a 180 nm SOI lateral P-I-N junction embedded shallow etched slab waveguide, as a function of TID, with pinch off occurring in the P-doped slab region at ~10 Mrad. (b) Simulated current-voltage response of the corresponding P-N junction as a function of TID. (c) Simulated change in effective modal index (Δn_{eff}) with change in applied voltage (ΔV), as a function of TID utilizing the Soref-Bennett equations. Image from [1].

5.2. Link-Level Design

A system architecture for the optical link has been conceived, allowing multiple silicon photonic (SiPho) based MRM devices to be optically connected in series, and dispersed throughout the inner pixel layer volume to connect to the front-end application specific integrated circuits (ASIC) and provide high-bandwidth optical readout (see Figure 5.5). The critical advantage of the conceived WDM scalable OI system architecture is that it allows for the highly sensitive optical components (e.g., laser sources, optical receivers, and high-speed electronics) to be placed outside of the high radiation environment (e.g., in the counting room), while only subjecting the SiPho MRM components to the extreme radiation levels in a remoted EOM configuration. This approach has additional advantages of (i) reducing energy consumption in the cooled pixel layer, (ii) allowing for remote wavelength control of the wavelength sensitive RRMs via external tunable laser sources to address radiation induced degradation over time, and (iii) increasing the optical link reliability by minimizing the number of components in the high radiation zone.

Remote operation of the MRMs is made possible by using Freedom Photonics' highly capable FP4209 InstaTune laser module, containing the broadband tunable laser and all required drive and control electronics to achieve high-speed arbitrary wavelength generation over a 40 nm range, centered at either the optical O-, C-, and U-band. The FP4209 module also contains the necessary microcontroller components to receive a feedback signal from the optical receiver, to maintain maximum OMA in the RRM by periodically adjusting the emission wavelength. The functionality of the FP4209 has been previously demonstrated in concert with a SiPho MRM [30]. Thus, the RadLink is well positioned to provide a critical element to the system architecture envisioned by Figure 5.5, which enables the remote control

of an MRM under varying environmental conditions, such as a temperature fluctuations and radiation induced damage [59], [60].

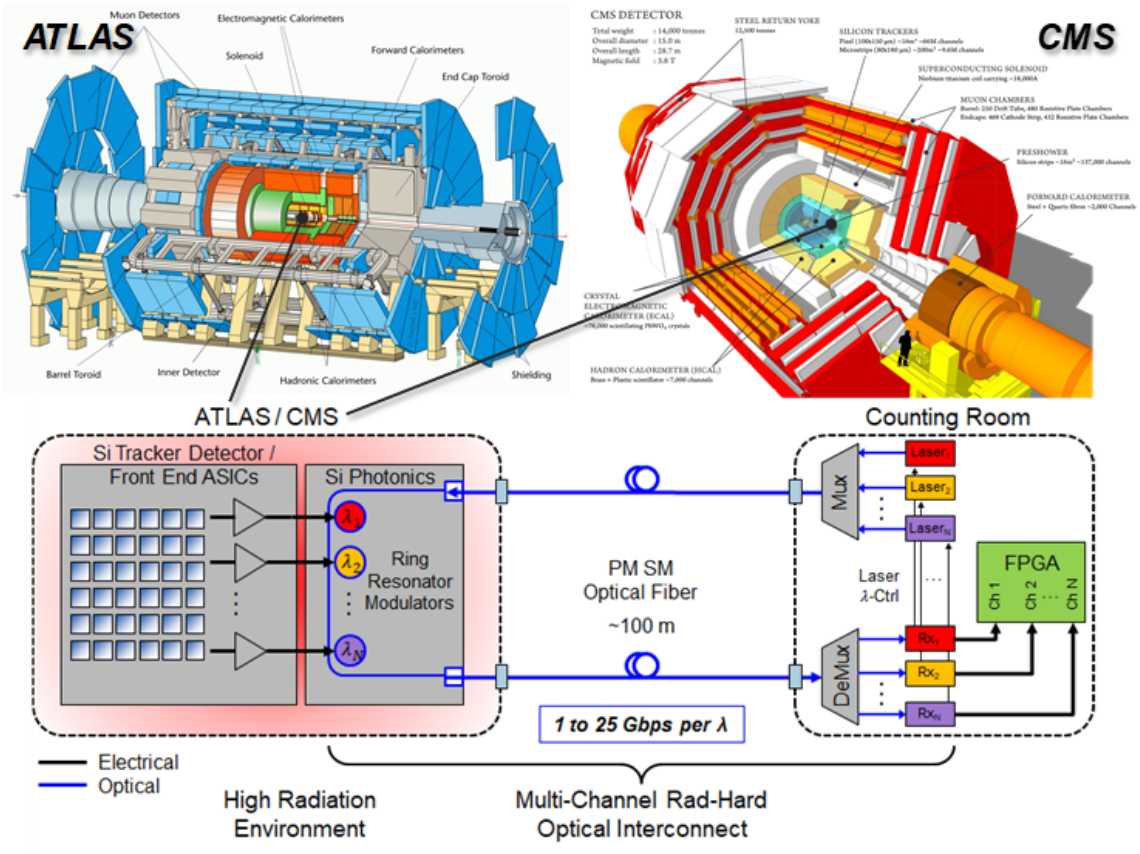

Figure 5.5. Overview of Freedom Photonics proposed highly scalable and radiation-hard optical link architecture, employing a remoted array of high-efficiency Si photonic (SiPho) ring resonator modulators (RRM). In this wavelength division multiplexed (WDM) optical link configuration, the laser sources and optical receivers are kept in the low radiation zone (e.g. counting room), while the SiPho RRMs are directly connected to front end ASICs of the pixel tracking detector. This novel optical link architecture will provide significant benefit for high energy physics (HEP) applications, and potentially also provides significant benefit to communication applications in basic energy science (BES), nuclear physics (NP), and fusion energy (FE). Image from [1].

Chapter 6 – SUMMARY & FUTURE WORK

In summary, a novel high-speed optical interconnect / link architecture has been developed in this thesis, which can be used in a harsh environment, such as at cryogenic temperatures or high radiation. This PhD dissertation addressed the challenges of optical interconnects for harsh environments in the following manner: (1) a novel and wavelength division multiplexed (WDM) scalable optical interconnect architecture has been developed—whereby the remoted EOM has been implemented as a microring resonator—and reduces both system complexity and energy consumption, (2) a high-speed optical link operating at cryogenic temperatures has been demonstrated—utilizing a silicon photonic based EOM—in addition to laser wavelength locking of the microring resonator, and (3) a semiconductor physics based model of the EOM has been developed to address the temperature dependent effects of the silicon p-n junction embedded in the microring resonator—based on the free-carrier plasma dispersion effect in doped silicon—to aid in the device design and optical interconnect link optimization for various harsh environment applications.

Future research work could focus on the following areas:

- Optimization of silicon photonic modulators for cryogenic and/or high radiation environments, based on custom doping profiles [32] and unique modulator topologies [62], [63]
- Optimization of optical interconnects for cryogenic and/or high radiation environments, based on driver and device co-design in monolithic platforms [38], [64]
- Development of full analytic expressions of temperature-dependent Soref-Bennett equations for more efficient design of devices
- Development of integrated receiver and laser wavelength controller circuit in a monolithic platform [38], [64], [65]

Appendix

A. Multi-Channel Optical Link Budget

Parameter			Value	Units
Optical Wavelength			1550	nm
Speed of Light			299792458	m/s
Electron Charge			1.60E-19	C
Planck			6.26E-34	J·s
Boltzmann			1.38E-23	J/K
Temperature			295	K

	Value			Units
Parameter / Channels	1	4	8	
Laser Source Average Output Power	10.00	10.00	10.00	mW
Laser Source Wall Plug Efficiency	0.25	0.25	0.25	-
Laser λ / T Control Circuit*	200.00	200.00	200.00	mW
Total Laser Electrical Power per Channel	240.00	240.00	240.00	mW
AWG Multiplexer Loss`	0.00	6.00	6.00	dB
Optical Fiber / Connector Coupling Loss	3.00	3.00	3.00	dB
Waveguide Propagation Loss	1.00	1.00	1.00	dB
Optical Power at Modulator	6.31	1.58	1.58	mW
Modulator Bias Point Loss	14.00	14.00	14.00	dB
Modulator Excess Loss	1.00	1.00	1.00	dB
Optical Modulator Switching Voltage	2.00	2.00	2.00	Vp-p
Optical Modulator Load Capacitance	50.00	50.00	50.00	fF
Channel Bitrate	2.50	2.50	2.50	Gbps
Modulator Energy per Bit	0.10	0.10	0.10	pJ
Total Link Energy per Bit**	96.10	96.10	96.10	pJ
Total Link Power per Channel	240.50	240.50	240.50	mW
Total Link Power	240.50	962.00	1924.00	mW
AWG DeMultiplexer Loss`	0.00	6.00	6.00	dB
Rx Responsivity	0.80	0.80	0.80	A/W
Rx Quantum Efficiency	0.64	0.64	0.64	-
Rx Average Photocurrent	100.71	1.60	1.60	μA
Bit Error Rate	1.E-12	1.E-12	1.E-12	-
Photons per Bit @ QL	27	27	27	-
Rx QL Sensitivity	-51.95	-51.95	-51.95	dBm
Rx Sensitivity Specification	-34.00	-34.00	-34.00	dBm
Received Power	125.89	2.00	2.00	μA
Received Power	-9.00	-27.00	-27.00	dBm
Link Margin	25.00	7.00	7.00	dB

*Assumes laser operation at ambient RT

**Includes laser and control circuitry

Bibliography

[1] Estrella, Steven B., Thomas P. Dorch, and Daniel S. Renner. "Progress in Optical Interconnects for Harsh Environments." *Physics and Simulation of Optoelectronic Devices XXX*. Vol. 11995. SPIE, 2022.

[2] "Silicon photonics market and technology report 2021", Yole Développement, May 2021, <https://s3.i-micronews.com/uploads/2021/05/YINTR21175-Silicon-Photonics-2021-Flyer.pdf> (11 January 2022).

[3] Rakowski, Michal, et al. "45nm CMOS-silicon photonics monolithic technology (45CLO) for next-generation, low power and high-speed optical interconnects." *Optical Fiber Communication Conference* (T3H-3). Optical Society of America, 2020.

[4] Wade, Mark, et al. "TeraPHY: A chiplet technology for low-power, high-bandwidth in-package optical I/O." IEEE Micro 40.2 (2020): 63-71.

[5] Soref, Richard. "The past, present, and future of silicon photonics." *IEEE Journal of selected topics in quantum electronics* 12.6 (2006): 1678-1687.

[6] Kittel, Charles. *Introduction to solid state physics*. Vol. 8. New York: Wiley, 1976.

[7] Lundstrom, Mark. *Fundamentals of carrier transport*. Cambridge university press, 2009.

[8] Khanna, Vinod Kumar. *Extreme-Temperature and Harsh-Environment Electronics; Physics, technology and applications, by Khanna, Vinod Kumar.* IOP ebooks. Bristol, UK: IOP Publishing, 2017.

[9] Varshni, Yatendra Pal. "Temperature dependence of the energy gap in semiconductors." *Physica* 34.1 (1967): 149-154.

[10] Bludau, W., A. Onton, and W. Heinke. "Temperature dependence of the band gap of silicon." *Journal of Applied Physics* 45.4 (1974): 1846-1848.

[11] Barber, H. D. "Effective mass and intrinsic concentration in silicon." *Solid-State Electronics*10.11 (1967): 1039-1051.

[12] Caiafa, A., et al. "Cryogenic study and modeling of IGBTs." *IEEE 34th Annual Conference on Power Electronics Specialist, 2003. PESC'03.* Vol. 4. IEEE, 2003.

[13] Pires, R. G., et al. "Carrier freezeout in silicon." *Cryogenics* 30.12 (1990): 1064-1068.

[14] Pieper, Ronald J., and Sherif Michael. "Comprehensive analytical approach to predicting freeze-out and exhaustion for uniform single-impurity semiconductors in equilibrium." *IEEE Transactions on Education* 48.3 (2005): 413-421.

[15] Soref, Richard A., and Brian R. Bennett. "Electrooptical effects in silicon." *IEEE journal of quantum electronics* 23.1 (1987): 123-129.

[16] Sze, Simon M., Yiming Li, and Kwok K. Ng. *Physics of semiconductor devices*. John wiley & sons, 2021.

[17] Ekin, Jack. *Experimental techniques for low-temperature measurements: cryostat design, material properties and superconductor critical-current testing*. Oxford university press, 2006.

[18] Neudeck, Gerold W. *The PN junction diode*. No. 2. Addison Wesley Publishing Company, 1983.

[19] Beckers, Arnout, Farzan Jazaeri, and Christian Enz. "Cryogenic MOS transistor model." *IEEE Transactions on Electron Devices* 65.9 (2018): 3617-3625.

[20] Gutierrez-D, Edmundo A., Jamal Deen, and Cor Claeys, eds. *Low temperature electronics: physics, devices, circuits, and applications*. Elsevier, 2000.

[21] Estrella, Steven B., Daniel Renner, Takako Hirokawa, Aaron Maharry, Mario Dumont, and Clint Schow. “High-Speed Optical Interconnect for Cryogenically Cooled Focal Plane Arrays.” 18.1, *GOMACTech*, 2019.

[22] Estrella, Steven B., Takako Hirokawa, Aaron Maharry, Daniel S. Renner, and Clint L. Schow. "High-speed silicon photonic optical interconnects for cryogenic readout (Conference Presentation)." *Optical Interconnects XX*. Vol. 11286. International Society for Optics and Photonics, 2020.

[23] Rabus, Dominik G. *Integrated ring resonators*. Springer-Verlag Berlin Heidelberg, 2007.

[24] Yariv, Amnon. "Universal relations for coupling of optical power between microresonators and dielectric waveguides." *Electronics letters* 36.4 (2000): 321-322.

[25] Yariv, Amnon. "Coupled-mode theory for guided-wave optics." *IEEE Journal of Quantum Electronics* 9.9 (1973): 919-933.

[26] Bogaerts, Wim, Peter De Heyn, Thomas Van Vaerenbergh, Katrien De Vos, Shankar Kumar Selvaraja, Tom Claes, Pieter Dumon, Peter Bienstman, Dries Van Thourhout, and Roel Baets. "Silicon microring resonators." *Laser & Photonics Reviews* 6.1 (2012): 47-73.

[27] Xu, Qianfan, Bradley Schmidt, Sameer Pradhan, and Michal Lipson. "Micrometre-scale silicon electro-optic modulator." *Nature* 435.7040 (2005): 325-327.

[28] Reed, Graham T., G. Mashanovich, F. Yand Gardes, and DJhttps Thomson. "Silicon optical modulators." *Nature Photonics* 4.8 (2010): 518-526.

[29] Shin, Myungjin, Yoojin Ban, Byung-Min Yu, Min-Hyeong Kim, Jinsoo Rhim, Lars Zimmermann, and Woo-Young Choi. "A linear equivalent circuit model for depletion-type silicon microring modulators." *IEEE Transactions on Electron Devices* 64.3 (2017): 1140-1145.

[30] Estrella, Steven B., Thomas P. Dorch, Trevor M. Cooper, Aaron Maharry, Takako Hirokawa, Daniel S. Renner, and Clint L. Schow. "Novel Link Architecture Minimizing Thermal Energy Dissipation for Cryogenic Optical Interconnects," in *Optical Fiber Communication Conference (OFC) 2021*, OSA Technical Digest (Optical Society of America, 2021), paper F2E.3.

[31] Holmes, D. Scott, Andrew L. Ripple, and Marc A. Manheimer. "Energy-efficient superconducting computing—Power budgets and requirements." *IEEE Transactions on Applied Superconductivity* 23.3 (2013): 1701610-1701610.

[32] Gehl, Michael, Christopher Long, Doug Trotter, Andrew Starbuck, Andrew Pomerene, Jeremy B. Wright, Seth Melgaard, John Siirola, Anthony L. Lentine, and Christopher DeRose. "Operation of high-speed silicon photonic micro-disk modulators at cryogenic temperatures." *Optica* 4.3 (2017): 374-382.

[33] Eltes, Felix, Gerardo E. Villarreal-Garcia, Daniele Caimi, Heinz Siegwart, Antonio A. Gentile, Andy Hart, Pascal Stark et al. "An integrated optical modulator operating at cryogenic temperatures." *Nature Materials* 19.11 (2020): 1164-1168.

[34] Sun, Zhipei, Amos Martinez, and Feng Wang. "Optical modulators with 2D layered materials." *Nature Photonics* 10.4 (2016): 227-238.

[35] Youssefi, Amir, Itay Shomroni, Yash J. Joshi, Nathan R. Bernier, Anton Lukashchuk, Philipp Uhrich, Liu Qiu, and Tobias J. Kippenberg. "A cryogenic electro-optic interconnect for superconducting devices." *Nature Electronics* 4.5 (2021): 326-332.

[36] Chakraborty, Uttara, Jacques Carolan, Genevieve Clark, Darius Bunandar, Gerald Gilbert, Jelena Notaros, Michael R. Watts, and Dirk R. Englund. "Cryogenic operation of silicon photonic modulators based on the DC Kerr effect." *Optica* 7.10 (2020): 1385-1390.

[37] Schultz, Kenneth I., et al., Lincoln Laboratory Journal 20, 2 (2014).

[38] Giewont, Ken, Karen Nummy, Frederick A. Anderson, Javier Ayala, Tymon Barwicz, Yusheng Bian, Kevin K. Dezfulian et al. "300-mm monolithic silicon photonics foundry technology." *IEEE Journal of Selected Topics in Quantum Electronics* 25.5 (2019): 1-11.

[39] Wu, Haonan, et al. "2.6 K VCSEL data link for cryogenic computing." *Applied Physics Letters* 119.4 (2021): 041101.

[40] Soós, C., et al. "Versatile Link PLUS transceiver development." *Journal of Instrumentation* 12.03 (2017): C03068.

[41] Zhang, Y., et al. "Key building blocks of a silicon photonic integrated transmitter for future detector instrumentation." *Journal of Instrumentation* 14.08 (2019): P08021

[42] de Cea, Marc, et al. "Photonic readout of superconducting nanowire single photon counting detectors." *Scientific Reports* 10.1 (2020): 1-8.

[43] Kim, M.H., Zimmermann, L. and Choi, W.Y., "A temperature controller IC for maximizing Si micro-ring modulator optical modulation amplitude," *Journal of Lightwave Technology*, vol. 37, no. 4, pp.1200-1206 (2019), doi: 10.1109/JLT.2018.2889899.

[44] Bardin, J.C., Sank, D., Naaman, O. and Jeffrey, E., "Quantum computing: An introduction for microwave engineers," *IEEE Microwave Magazine*, vol. 21, no. 8, pp.24-44 (2020), doi: 10.1109/MMM.2020.2993475.

[45] Wang, J., Sciarrino, F., Laing, A. and Thompson, M.G., "Integrated photonic quantum technologies," *Nature Photonics*, vol. 14, no. 5, pp.273-284 (2020), doi: 10.1038/s41566-019-0532-1.

[46] Bahadori, Meisam, Sébastien Rumley, Dessislava Nikolova, and Keren Bergman. "Comprehensive design space exploration of silicon photonic interconnects." *Journal of Lightwave Technology* 34.12 (2016): 2975-2987.

[47] Fard, E.M., Long, C.M., Lentine, A.L. and Norwood, R.A., "Cryogenic C-band wavelength division multiplexing system using an AIM Photonics Foundry process design kit," *Optics Express*, vol. 28, no. 24, pp. 35651-35662 (2020), doi: 10.1364/OE.404617.

[48] Komma, J., Schwarz, C., Hofmann, G., Heinert, D. and Nawrodt, R., “Thermo-optic coefficient of silicon at 1550 nm and cryogenic temperatures,” *Applied Physics Letters*, vol. 101, no. 4, p. 041905 (2012), doi: 10.1063/1.4738989.

[49] Black, Eric D. "An introduction to Pound–Drever–Hall laser frequency stabilization." *American journal of physics* 69.1 (2001): 79-87.

[50] Padmaraju, Kishore, Dylan F. Logan, Takashi Shiraishi, Jason J. Ackert, Andrew P. Knights, and Keren Bergman. "Wavelength locking and thermally stabilizing microring resonators using dithering signals." *Journal of Lightwave Technology* 32.3 (2013): 505-512.

[51] Zortman, William A., Anthony L. Lentine, Douglas C. Trotter, and Michael R. Watts. "Bit-error-rate monitoring for active wavelength control of resonant modulators." *IEEE Micro* 33.1 (2012): 42-52.

[52] Wang, Zhao, Dixon Paez, Ahmed I. Abd El-Rahman, Peng Wang, Liam Dow, John C. Cartledge, and Andrew P. Knights. "Resonance control of a silicon micro-ring resonator modulator under high-speed operation using the intrinsic defect-mediated photocurrent." *Optics Express* 25.20 (2017): 24827-24836.

[53] Cox, Jonathan A., Anthony L. Lentine, Douglas C. Trotter, and Andrew L. Starbuck. "Control of integrated micro-resonator wavelength via balanced homodyne locking." *Optics express* 22.9 (2014): 11279-11289.

[54] Yin, Bozhi, Hayk Gevorgyan, Deniz Onural, Anatol Khilo, Miloš A. Popović, and Vladimir M. Stojanović. "Electronic-Photonic Cryogenic Egress Link." In *ESSCIRC 2021-IEEE 47th European Solid State Circuits Conference (ESSCIRC)*, pp. 51-54. IEEE, 2021.

[55] Pernice, Wolfram HP, Carsten Schuck, Mo Li, and Hong X. Tang. "Carrier and thermal dynamics of silicon photonic resonators at cryogenic temperatures." *Optics express* 19.4 (2011): 3290-3296.

[56] S. Bhandaru, S. Hu and D. M. Fleetwood, "Total ionizing dose effects on silicon ring resonators," *IEEE Transactions on Nuclear Science*, vol. 62, no. 1, pp. 323-328, 2015.

[57] S. S. E. Nasr-Storey, et al. "Effect of radiation on a Mach-Zehnder interferometer silicon modulator for HL-LHC data transmission applications," *IEEE Transactions on Nuclear Science*, vol. 62, no. 1, pp. 329-335, 2015.

[58] Hoffman, Galen B., M. Gehl, N. J. Martinez, D. C. Trotter, A. L. Starbuck, A. Pomerene, C. M. Dallo et al. "The effect of gamma radiation exposure on active silicon photonic device performance metrics." *IEEE Transactions on Nuclear Science* 66.5 (2019): 801-809.

[59] Zeiler, Marcel, S. Detraz, L. Olantera, C. Sigaud, C. Soos, J. Troska, and F. Vasey. "A system-level model for high-speed, radiation-hard optical links in HEP experiments based on silicon Mach-Zehnder modulators." *Journal of Instrumentation* 1.12 (2016): C12059.

[60] Ahmed, Zeeshan, Lonnie T. Cumberland, Nikolai N. Klimov, Ileana M. Pazos, Ronald E. Tosh, and Ryan Fitzgerald. "Assessing radiation hardness of silicon photonic sensors." *Scientific Reports* 8.1 (2018): 1-7.

[61] Tzintzarov, George N., Adrian Ildefonso, Patrick S. Goley, Milad Frounchi, Delgermaa Nergui, Sunil G. Rao, Jeffrey Teng et al. "Electronic-to-Photonic Single-Event Transient Propagation in a Segmented Mach–Zehnder Modulator in a Si/SiGe Integrated Photonics Platform." *IEEE Transactions on Nuclear Science* 67.1 (2019): 260-267.

[62] Yariv, Amnon. "Critical coupling and its control in optical waveguide-ring resonator systems." *IEEE Photonics Technology Letters* 14.4 (2002): 483-485.

[63] Sacher, W. D., W. M. J. Green, S. Assefa, T. Barwicz, H. Pan, S. M. Shank, Y. A. Vlasov, and J. K. S. Poon. "Coupling modulation of microrings at rates beyond the linewidth limit." *Optics express* 21.8 (2013): 9722-9733.

[64] Li, Hao, Ganesh Balamurugan, Taehwan Kim, Meer N. Sakib, Ranjeet Kumar, Haisheng Rong, James Jaussi, and Bryan Casper. "A 3-D-integrated silicon photonic microring-based 112-Gb/s PAM-4 transmitter with nonlinear equalization and thermal control." *IEEE Journal of Solid-State Circuits* 56.1 (2020): 19-29.

[65] Tan, Min, Kaixuan Ye, Da Ming, Yuhang Wang, Zhicheng Wang, Li Jin, and Junbo Feng. "Towards electronic-photonic-converged thermo-optic feedback tuning." *Journal of Semiconductors* 42.2 (2021): 023104.